Astronomy & Astrophysics manuscript no. aruiz˙SEDhlirgs
March 3, 2010

© ESO 2010

arXiv:1003.0800v1 [astro-ph.CO] 3 Mar 2010

Spectral Energy Distribution of Hyper-Luminous Infrared Galaxies

A. Ruiz[1,2], G. Miniutti[3], F. Panessa[4], and F.J. Carrera[1]

[1] Instituto de Física de Cantabria (IFCA), CSIC-UC, Avda. de los Castros, 39005 Santander, Spain
[2] Istituto Nazionale di Astrofisica (INAF), Osservatorio Astronomico di Brera, via Brera 21, 20121 Milano, Italy
[3] LAEX, Centro de Astrobiología (CSIC-INTA); LAEFF, P.O: Box 78, E-28691 Villanueva de la Cañada, Madrid, Spain
[4] Istituto Nazionale di Astrofisica (INAF), IASF-Roma, Via Fosso del Cavaliere 100, I-00133 Rome, Italy
e-mail: `angel.ruiz@brera.inaf.it`

Received March 31, 2009; accepted March 2, 2010

ABSTRACT

Aims. The relationship between star formation and super-massive black hole growth is central to our understanding of galaxy formation and evolution. Hyper-Luminous Infrared Galaxies (HLIRGs) are unique laboratories to investigate the connection between starburst (SB) and Active Galactic Nuclei (AGN), since they exhibit extreme star formation rates, and most of them show evidence of harbouring powerful AGN.
Methods. Our previous X-ray study of a sample of HLIRGs shows that the X-ray emission of most of these sources is dominated by AGN activity. To improve our estimate of the relative contribution of the AGN and SB emission to its total bolometric output, we have built multi-wavelength (from radio to X-rays) spectral energy distributions (SEDs) for these HLIRGs, and we have fitted standard empirical AGN and SB templates to these SEDs.
Results. In broad terms, most sources are well fitted using this method, and we found AGN and SB contributions similar to those obtained by previous studies of HLIRGs. We have classified the HLIRGs SEDs in two groups, named class A and class B. Class A HLIRGs show a flat SED from the optical to the infrared energy range. Three out of seven class A sources can be modelled with a pure luminosity-dependent QSO template, while the rest of them require a type 1 AGN template and a SB template. The SB component is dominant in three out of four class A objects. Class B HLIRGs show SEDs with a prominent and broad IR bump. These sources can not trivially be modelled with a combination of pure AGN and pure SB, they require templates of composite objects, suggesting that $\gtrsim 50\%$ of their emission comes from stellar formation processes.
Conclusions. We propose that our sample is actually composed by three different populations: very luminous QSO (class A objects with negligible SB contribution), young galaxies going through their maximal star formation period (class A objects with significant SB emission) and the high luminosity tail of ULIRG population distribution (class B sources).

Key words. galaxies: active – galaxies: starburst – galaxies: evolution – X-rays: galaxies – infrared: galaxies

1. Introduction

During the last decade, the hypothesis that Active Galactic Nuclei (AGN) and galaxy formation and evolution are closely related has been supported by a growing body of observational evidences. On one hand, most galaxies have been shown to harbour a central super-massive black hole (Kormendy & Gebhardt 2001) whose mass is correlated with that of the host galaxy spheroid (Magorrian et al. 1998; McLure & Dunlop 2002) and, on the other hand, the evolution of cosmic star formation and of luminous AGN activity appear rather similar (Franceschini et al. 1999; Silverman et al. 2005). These hints clearly suggest a connection between the growth of the central black hole through accretion and the growth of the spheroid through star formation.

The observational study of these two phenomena needs penetrating radiation like X-rays, mid-infrared (MIR), far-infrared (FIR) or sub-mm. On one hand, star formation takes place in heavily obscured environments. Primary radiation is then reprocessed by dust and re-emitted in the MIR-FIR band. X-ray emission from starburst (SB) activity is enhanced by energetic phenomena related to the final stages of stellar evolution, e.g. supernova remnants or X-ray binaries (Persic & Rephaeli 2002). On the other hand, X-ray emission is the signature of AGN activity, produced by black hole (BH) growth through accretion. However, synthesis models of the X-ray background require that most AGNs in the Universe are obscured (Ueda et al. 2003; Gilli et al. 2007), i.e. most of the accretion power in the Universe is absorbed and then re-emitted in the infrared (IR) bands (Fabian & Iwasawa 1999).

IR and X-ray observations are therefore essential to understand the phenomena of star formation and AGN, as well as their interplay and connection. Fortunately, nowadays we have powerful tools to observe the Universe in both energy ranges, like *Chandra*, XMM-*Newton*, *Spitzer*, AKARI or *Suzaku*. Different strategies can be employed to investigate the IR/X-ray synergy and its effect on the AGN-galaxy co-evolution, e.g. by multi-wavelength surveys like GOODS, AEGIS or COSMOS (Dickinson et al. 2003; Davis et al. 2007; Scoville et al. 2007), by targeted MIR observations of peculiar X-ray sources like X-ray absorbed broad line QSO (Stevens et al. 2005; Page et al. 2007), and by targeted X-ray observations of MIR/FIR-emitting objects like Ultraluminous Infrared Galaxies (ULIRGS, Franceschini et al. 2003; Teng et al. 2005) or Hyperluminous Infrared Galaxies (HLIRGS, Wilman et al. 1998; Ruiz et al. 2007).

ULIRGs are a family of galaxies with IR luminosity $L_{\rm IR} \geq 10^{12}\ L_{\odot}$, whose bolometric output is dominated by the emission in the IR waveband (see Lonsdale et al. 2006 for a complete review). X-ray and IR data clearly suggest that these sources are powered by SB and, in some cases ($\sim$ 50%), by

AGNs (Farrah et al. 2003; Franceschini et al. 2003; Teng et al. 2005; Nardini et al. 2008). The fraction of ULIRGs hosting an AGN increases with increasing IR luminosity (Veilleux et al. 1995, 1999). Most of these objects are in interacting systems, i.e. ULIRGs are most likely triggered by mergers of galaxies (Farrah et al. 2001; Veilleux et al. 2002).

HLIRGs present an IR luminosity $L_{\rm IR} \geq 10^{13}\ L_{\odot}$. These are among the most luminous objects in the Universe. Assuming that the FIR emission above 50 μm is dominated by SB, their estimated star formation rates (SFR) are $\gtrsim 1000\ M_{\odot}\ {\rm yr}^{-1}$ (Rowan-Robinson 2000). IR and optical observations support that most harbour an AGN (Verma et al. 2002; Farrah et al. 2002a), although the main power source is still controversial. As HLIRGs could represent the most vigorous stage of galaxy formation, they are unique laboratories to investigate extremely high stellar formation, and its connection to super-massive black hole growth.

Only about a third of HLIRGs are located in interacting systems (Farrah et al. 2002b), so a considerable number of these objects can not be classified just as objects in the brightest end of the ULIRG population. They could be very young galaxies experiencing their major episode of star formation (Rowan-Robinson 2000), or may be a completely new class of objects, e.g. a transient IR-luminous phase in quasar evolution (Farrah et al. 2002a; Stevens et al. 2005).

X-rays are a very convenient tool to disentangle the relative contribution of SB and AGN to the total output of HLIRGs. Only a few of these objects had been studied in X-rays (Wilman et al. 1998, 2003; Iwasawa et al. 2005) before Ruiz et al. (2007) presented the first systematic study of these sources in the X-ray band.

A sample of 14 HLIRGs was observed by XMM-*Newton* and 10 were detected (Ruiz et al. 2007). All of them show an AGN-dominated X-ray spectrum. We find X-ray thermal emission associated with SB for just one source, while all ULIRGs show a SB component in their X-ray spectra (Franceschini et al. 2003). The much brighter AGN emission probably hides the X-rays originated in the SB (if this component actually exists). The IR luminosity of most HLIRGs of the sample is consistent with an AGN origin, but it is systematically over that expected for a local QSO (Elvis et al. 1994; Risaliti & Elvis 2004) of the same X-ray luminosity. This IR excess could be due to X-ray obscuration, SB emission or may be due to an intrinsic difference between the spectral energy distribution (SED) of AGN in HLIRGs and the SED of local QSO.

To clarify these questions a proper study of the SED of these objects is needed. Several studies of HLIRGs SED have been published (Rowan-Robinson 2000; Verma et al. 2002; Farrah et al. 2002a), but they were always limited to the IR energy range. These studies apply a two component model (AGN+SB) to reproduce the IR emission, using radiative transfer models (RTM) for the AGN dust torus (Efstathiou & Rowan-Robinson 1995; Rowan-Robinson 1995) and the SB (Efstathiou et al. 2000) components. Rowan-Robinson (2000) studied a sample of 45 HLIRGs, finding a continuum distribution in the relative contribution of the AGN and SB components, from pure starburst to pure AGN, with most objects being composite. On the other hand, Farrah et al. (2002a) selected a complete sample of HLIRGs in a manner independent of obscuration, inclination or AGN content and included sub-mm data (sub-mm data introduce a tight constraint on the SB luminosities), finding that all HLIRGs in the sample were composite objects.

In this paper we present a study of HLIRGs SED with two majors improvements and one limitation compared with the earlier studies commented above: (a) we have greatly enlarged the wavelength coverage, from radio to X-rays, and (b) we have significantly increased the photometric data coverage. However, as a self consistent analytical model able to reproduce the whole SED at so broad frequency range would be very complex to compute (and beyond the scope of this paper), we have compared our constructed SEDs with empirical AGN and SB templates, instead of using analytical RTM as in previous studies.

The paper is organized as follows. Section 2 briefly describes the HLIRG sample. Section 3 explains how we built the SED and the data used to this end, and Sect. 4 the methods we have employed to model the SEDs. Results are presented in Sect. 5, compared with previous studies of HLIRGs in Sect. 6 and discussed in Sect. 7. Section 8 summarizes our conclusions.

The *Wilkinson Microwave Anisotropy Probe* (*WMAP*) concordance cosmology has been adopted throughout this paper: $H_0 = 70$ km s^{-1} Mpc^{-1}, $\Omega_m = 0.27, \Omega_\Lambda = 0.73$ (Spergel et al. 2003).

2. The HLIRG sample

The sample studied here is the one investigated in Ruiz et al. (2007). From the Rowan-Robinson (2000) sample of HLIRGs we selected those sources with public data available in the XMM-*Newton* Science Archive as of December 2004, and we added our own XMM-*Newton* AO-5 observations.

We limited this sample to sources with redshift less than $\sim$ 2 to avoid strong biasing towards high redshift quasars. Nevertheless, selecting the sample by using the availability of X-ray data probably introduces a selection effect in favour of the presence of an AGN. We also rejected one source from the original sample, IRAS 13279+3401. Using recent optical and MIR spectra, we have determined its redshift to be $z \sim 0.02$ (see Appendix A), much lower than the one presented in the literature ($z = 0.36$, Rowan-Robinson 2000). Therefore, our estimate of its IR luminosity is $3 \times 10^{10}\ L_{\odot}$, even below that necessary to classify it as a LIRG. Hence, we have thirteen objects in our final sample (see Table 1).

According to their optical spectra (derived from the literature), two sources are classified as starburst galaxies and twelve sources present AGN features. Among the latter eight are classified as 'type I', and four of them as 'type II'. All type II and one NL-SB galaxy are Compton-Thick (CT) candidates. See Ruiz et al. (2007) for a further discussion on this sample.

3. Data compilation

Our goal is to construct a well sampled SED for each object in a broad frequency range, from radio to X-rays. To this end, we have carefully searched in the literature and in several astronomical databases. See Appendix B for a complete description on the origin of the photometry data for each HLIRG.

All data included in the SEDs (presented in Tables B.1-B.13, see Appendix B) have been converted to monochromatic flux density units, corrected for the Galactic reddening and blueshifted to rest-frame.

3.1. Radio

Most of the HLIRGs in the sample have at least one observation in the radio range. These data come from different observations by VLA, ATCA, IRAM and other radio-telescopes.

3.2. Infrared

Our sources are well observed in the IR band. There are photometric data from *IRAS* (Point Source Catalogue, Joint IRAS Science Working Group 1988; Faint Source Catalogue, Moshir et al. 1990) or *ISO* for all the objects. Most of them also have been observed with SCUBA in the sub-mm band (Farrah et al. 2002a).

In addition, there are public *Spitzer* MIR data for several sources: IRAC photometric data and IRS spectra. We have reduced the IRAC data and we made our own photometric measurements. We have re-binned the IRS spectra of our HLIRG in broad bands, avoiding known emission and absorption features (a further analysis of these MIR spectra will be presented in Ruiz et al., in preparation). Most of these sources also have NIR data from the 2MASS survey[1] (Cutri et al. 2003).

3.3. Optical and UV

Most of the optical data were obtained from the Sloan Digital Sky Survey-Data Release 5[2] (SDSS-DR5, Adelman-McCarthy et al. 2007) and SuperCOSMOS Sky Survey[3] (SSS). A few data in V and B bands were taken from the XMM-*Newton* Optical Monitor (OM).

We have only a few data in the UV range, mostly from the OM. Other data come from IUE and FUSE observations.

3.4. X-ray

The XMM-Newton spectra previously studied in Ruiz et al. (2007) are available. We have corrected each X-ray spectrum for the line of sight Galactic absorption (Dickey & Lockman 1990) and we have re-binned the data in just a few energy bands[4]. In addition, the X-ray and the OM data come from simultaneous observations, allowing us to check any variability effects.

3.5. Overall description of the SEDs

Figure 1 shows the SEDs we have built for our sources. We have divided the sample in two classes accordingly to their optical spectral classification. On one hand we grouped objects classified as type I AGN (named class A sources) and on the other hand objects classified as type II AGN and SB (named class B sources).

From a purely phenomenological point of view, class A and B sources seem to show a different SED shape. Class A objects have a SED approximately flat from the FIR to the optical range (the typical shape of quasars' SED), while class B objects show a prominent broad IR bump dominating the emission over the rest of the spectrum.

To check if the above distinction holds quantitatively, we compared the distribution of X-ray-to-IR and optical-to-IR flux ratios for class A and class B sources. We estimated the monochromatic fluxes at three different rest-frame wavelengths, in the IR (30 μm), optical (4400 Å) and X-rays (2 keV) through a linear interpolation of the SED (these points lie in well-sampled regions of the SEDs, so these are reasonable estimates of the continua at those energies). Fig 2 shows the distribution of the X-ray-to-IR ($F_{\rm X}/F_{\rm IR}$) and optical-to-IR ($F_{\rm opt}/F_{\rm IR}$) flux ratios for the class A (blue histogram) and class B (pink histogram) sources. The distributions seem to be different for both classes of HLIRGs. By using a Kolmogorov-Smirnov test, the probability that class A and class B samples come from different parent populations is 92.6% for the $F_{\rm X}/F_{\rm IR}$ distribution and $\sim$ 99.7% for the $F_{\rm opt}/F_{\rm IR}$ distribution.

This rough analysis of the SED properties is clearly limited, but the results seem to support our classification of HLIRGs in two classes. We suggest that, since the SED classification is directly related to the optical spectra classification, the distinct SED shape of HLIRGs could be explained by different levels of obscuration in the line of sight and/or the relative contribution of the SB emission to the total output.

4. SED fitting

Once all the SEDs were built, our aim was to check for the presence of AGN and/or SB emission in these sources and estimate the contribution of these components to the total output. We fitted all SEDs by using the χ^2 minimization technique with a simple model based on the use of convenient templates (see Sect. 4.1 for details). The fitting procedure and the SED templates were implemented using the modelling and fitting tool `Sherpa` (Freeman et al. 2001), included in the software package CIAO 3.4[5].

Our model comprises two additive components, one associated to the AGN emission and the other associated to the SB emission. We can express this model as follows:

$$F_\nu = F_{\rm BOL}\left(\alpha\, u_\nu^{\rm AGN} + (1-\alpha)\, u_\nu^{\rm SB}\right), \qquad (1)$$

where $F_{\rm BOL}$ is the total bolometric flux, α is the relative contribution of the AGN to $F_{\rm BOL}$, F_ν is the total flux at the frequency ν, while $u_\nu^{\rm AGN}$ and $u_\nu^{\rm SB}$ are the normalized AGN and SB templates (i.e., the value of the integral over the whole range of frequencies is unity for each SED template). This model contains only two free parameters, $F_{\rm BOL}$ (the normalization) and α. The bolometric luminosity can be estimated as $L_{\rm BOL} = 4\pi D_L^2 F_{\rm BOL}$, where D_L is the luminosity distance.

The model we are adopting to fit the SED is somehow rough and does not provide a precise description of the SED features, so we expect a poor fit in terms of χ^2 value. However, the entire SED shape, from the radio to soft gamma rays, depends on a large number of physical parameters which produce different SED shapes even among the same class of sources (AGN, SB, etc.). Moreover, the impact of the different individual physical quantities on the overall SED and, perhaps most importantly, the effect of their interplay and interaction on the overall SED shape is far from being robustly settled from a theoretical point of view. The development of an analytical or semi-analytical model would be of great importance, but given that such models are difficult to build and likely not unique, they clearly are beyond the scope of this work. We propose instead the simpler template-fitting approach to discriminate, as a zeroth-order approximation, the relative component contribution (AGN and/or SB) to the overall bolometric luminosity of each source.

We have chosen the fit with the lowest reduced χ^2 as our "best fit" model. As we said above, the value of $\chi^2/\mathrm{d.o.f.} >> 1$ even for these best fits. Nevertheless, this quantity varies significantly for most sources between the different combinations of templates we tested during the χ^2 minimization process. In those objects where different types of templates obtained similar χ^2 values, we have chosen the template most consistent with previous results in the literature.

---

[1] http://www.ipac.caltech.edu/2mass/

[2] http://www.sdss.org/dr5

[3] http://www-wfau.roe.ac.uk/sss/

[4] Through our X-ray data reduction we did not detect the source IRAS 14026+4341. Even so, this source has a counterpart in the 2XMMi catalogue (Watson et al. 2009). We have considered the five energy band fluxes as in the 2XMMi catalogue.

[5] http://cxc.harvard.edu/ciao3.4/

Our templates were chosen to minimize the contribution of the host galaxy's non-SB stellar emission (see Sect. 4.1), but there could still be a remnant of this emission in the templates. Therefore, by adding two different templates we could have summed twice this stellar emission. We checked this effect adding a stellar template to the model[6]. The normalization of this component was free and negative, in order to subtract the "second" stellar contribution. The addition of the new component did not change the final results of the SED fitting, so we can reject any important stellar contamination in our templates.

4.1. Templates

The templates we have employed to model the SEDs of our sources are empirical SEDs of well observed SB and Seyfert (Sy) galaxies in the local universe (see Table 2).

To reproduce the AGN contribution we used six AGN templates:

1. Two mean SED of radio quiet local QSO (Fig. 3(a)): a luminosity independent SED (Elvis et al. 1994; Richards et al. 2006) and a luminosity-dependent one (Hopkins et al. 2007). The latter template is similar to the standard SED of QSO from Elvis et al. (1994), but the value of $\alpha_{\rm OX}$ depends on the bolometric luminosity (Steffen et al. 2006), and the X-ray emission above 0.5 keV is modelled by a power law ($\Gamma = 1.8$) with a cut-off at 500 keV and a reflection component generated with the `PEXRAV` model (Magdziarz & Zdziarski 1995). Therefore, this template has two parameters: normalization (the bolometric flux of the AGN) and redshift. For a given flux and redshift, the bolometric luminosity is calculated and, hence, the value of $\alpha_{\rm OX}$. The first parameter was left free to vary during the fitting, while the second was fixed accordingly to the redshifts obtained in the literature.
2. Four Sy2 galaxies (Fig. 3(b)): these objects have hydrogen column densities ($N_{\rm H}$) varying from 10^{22} cm^{-2} (Compton thin objects) to greater than 10^{25} cm^{-2} (Compton thick objects). They were selected from a sample of Sy2 galaxies with minimal starburst contribution (Bianchi et al. 2006). The AGN templates show two bumps, in the FIR and in the NIR-optical, except for the AGN3 template, which only present a broad IR bump. The differences between them are the relative height of these bumps, the position of their peaks and the ratio between the optical and X-ray fluxes.

To represent the SB contribution we have chosen a set of four starburst galaxies well observed in the full spectral range (Fig. 4(a)). We have tried to cover a broad range of burst ages, dust contents and SFR. These physical properties are reflected in the SEDs showing different levels of obscuration, width and wavelength peaks.

1. NGC 5253 is a low-metallicity star-forming dwarf galaxy. Its nucleus is the site of a highly obscured and extremely young (< 10 Myr) burst of star formation (Beck et al. 1996), with a SFR$\sim 8\ M_\odot$ yr^{-1}.
2. NGC 7714 is a young unobscured SB (Brandl et al. 2004) with SFR$\sim 6\ M_\odot$ yr^{-1} and a burst age between 3-5 Myr (Gonzalez-Delgado et al. 1995).
3. M82 is an evolved pure SB galaxy with SFR$\sim 10\ M_\odot$ yr^{-1} (Strickland et al. 2004).
4. IRAS 12112+0305 is a bright ULIRG powered by SB and with severe limits to any AGN contribution (Imanishi et al. 2007; Nardini et al. 2008). The estimated SFR for this object is $\sim 600\ M_\odot$ yr^{-1} (Franceschini et al. 2003).

All of them show two bumps, peaking in the FIR and in the NIR-optical. The main difference between the templates is the relative height between these bumps and their widths.

We included four SED templates built from sources which they harbour both an AGN and a SB (Fig. 4(b)):

1. NGC 1068 is a Sy2 galaxy with a composite nature, i.e. it harbours a heavily buried AGN ($N_{\rm H} > 10^{25}$ cm^{-2}, Matt et al. 1997) and also an intense SB (Telesco et al. 1984). The bolometric luminosity of this object is roughly evenly divided between the two component. The SB emission dominates longward of 30 μm and the AGN dominates shortward of 20-10 μm.
2. Mrk 231 is an ULIRG ($L_{\rm IR} = 3.2 \times 10^{12}$) optically classified as a Broad Absorption Line QSO (Berta 2005) with a massive young nuclear SB which is responsible for 25%-40% of the nuclear bolometric luminosity (Davies et al. 2004).
3. IRAS 19254-7245, the "Superantennae", is a double-nucleated ULIRG optically classified as a Sy2 galaxy, with intense star formation. The AGN contribution to the total output is $\sim 40-50\%$ (Berta et al. 2003).
4. IRAS 22491-1808 is a Sy2 ULIRG (Berta 2005) where the AGN emission is $\sim$ 70% of the bolometric luminosity (Farrah et al. 2003).

We fitted these composite templates to those HLIRGs where the initial AGN+SB model was insufficient to reproduce the data (see Sect. 5.2).

We extracted the photometric data for the templates using VOSED[7] and VOSpec[8] software. These utilities use Virtual Observatory (Quinn et al. 2004) tools to extract photometric and spectral data from several astronomical archives and catalogues. The templates were improved with data from NED database in wavelength ranges where VOSED and VOSpec provided no data. These objects are well observed at all the frequency ranges, particularly in the NIR and optical bands. We rejected some redundant data and we tried to extract only the nuclear emission to avoid as much contamination from the host galaxy as possible. To this end we have chosen only those data with a roughly constant aperture within the nucleus of the galaxy.

5. Results

Figures 5 and 6 show the SED[9] and the best fit model selected for each object, and Table 1 summarizes the results of our analysis. See Sect. 5.4 for comments on some particular sources.

5.1. Class A HLIRGs

We have shown that our simple two-component SED model is a fair approximation for most of these HLIRGs (see Fig. 1(a)). We found that all class A HLIRGs but one (IRAS 14026+4341, see Sect. 5.4 below) are well fitted with type I AGN templates, consistent with their optical classification, and an additional SB component is required in three objects. The AGN component dominates the bolometric output in four out of these six sources, while two objects present a powerful SB component, with 60%-70% contribution of the bolometric luminosity.

---

[6] The SED of the elliptical galaxy M 87 was employed to model the stellar emission.

[7] http://sdc.laeff.inta.es/vosed

[8] http://esavo.esa.int/vospec

[9] Several photometric points are upper limits. The most conservative approach was chosen for the fit. We set the point to zero and the upper error bar to the upper limit value.

We have then 3 sources with a SB-dominated SED (IRAS F12509+3122, IRAS 14026+4341 and IRAS F14218+3845), one AGN-dominated source with an important SB contribution (IRAS 18216+6418), and 3 objects which seem to be extremely luminous quasars with no particular differences from the local ones, judging from their SEDs and X-ray spectra (Ruiz et al. 2007).

A noticeable result for the class A HLIRGs is that the AGN1 template over-predicts the X-ray flux of these sources, as found in our previous X-ray analysis. These discrepancies in the X-ray band can not be related to variability effects, since the OM data, simultaneous to the X-ray observations, match well with other optical and UV data obtained in different epochs. When we modelled these objects with the luminosity-dependent AGN1-L SED template, we found a significant improvement in the fit in terms of χ^2 for most sources (4 out of 6) and the X-ray emission is better predicted. This result is consistent with the known $\alpha_{\rm OX}$ luminosity relationship (Strateva et al. 2005; Steffen et al. 2006; Kelly et al. 2008).

We must also note that the IR-to-bolometric ratio of these sources is within $\sim 40-70\%$, so an important fraction of their bolometric output is not emitted in the IR range. Hence, strictly speaking, they should not be considered as HLIRGs, particularly those with a completely AGN-dominated SED, where less than 50% of their bolometric luminosity is in the IR. This “contamination” can be expected given the selection criteria of the Rowan-Robinson (2000) parent sample, which simply selected those known sources with $L_{\rm IR} \gtrsim 10^{13}\ L_\odot$.

5.2. Class B HLIRGs

We found that these sources are fitted with a dominant SB component and, in most cases, a minor AGN contribution (< 10%). However our model present some problems for class B HLIRGs that we did not find in class A objects (see Fig. 6):

1. The level of obscuration in the observed X-ray spectra is higher than the one expected from the AGN templates.
2. Most sources show an excess in the MIR-NIR band not modelled by these templates, i.e. the width of the IR bump seems to be broader than the bumps in the starburst templates.
3. The peak of the template does not match the IR peak of the SEDs in several sources.

In order to improve the fit quality for the class B sources, we repeated the SED fitting using a set of templates from composite sources (see Sect. 4.1), where both AGN and SB emission are significant. By using these composite templates, we found that the statistical quality of our fits was significantly improved for all but one case (IRAS F15307+3252, see Sect. 5.4 below). For most objects, the χ^2 obtained with any of the composite templates is significantly lower than the χ^2 obtained with any combination of pure AGN and pure SB templates. CP1 is the best fit template for 4 out of 6 sources, consistent with their spectral classification (type 2 AGN) and X-ray obscuration level (Compton-Thick). Two sources are best fitted with the CP2 template.

IRAS F00235+1024 is the only source that still shows a significant IR excess, which suggest that the SB contribution may be larger in this source that in the CP1 template (~ 50%).

5.3. Fitting without X-ray data

In order to check how much X-ray data influence the SED fitting results, we exclude X-ray data from the SED fitting procedure. Class A sources are still well represented by the same models (see Table 1, columns labeled as “no X-rays”), while class B galaxies are preferentially fitted with an AGN3 template (Compton thin model) and a SB component. Moreover, the AGN contribution grows significantly in most sources, particularly in the class B sources. When X-rays are included, a severe limit is imposed and the AGN contribution decreases dramatically. This shows that X-rays are important to obtain an accurate model with our technique and, hence, a better estimation of the contribution of each component to the total output.

5.4. Notes on particular sources

IRAS 14026+4341

This source is optically classified as a type I AGN (Rowan-Robinson 2000), in agreement with the SDSS classification, and recent MIR *Spitzer* data also suggest the presence of an AGN in this object (Ruiz et al., in preparation), but our best fit model is obtained by using the SB2 template. The X-ray data impose a severe constraint, rejecting the AGN templates that predict a higher emission in the X-ray band. If we fit again this SED using no X-ray data (see Sect. 5.3) we find that the best fit is obtained by AGN1+SB2.

The X-ray emission of this source seems to be affected by absorption (see Fig. 5(d)): it is not detected in the soft X-ray band (0.5-2 keV) and its 2XMMi hardness ratio ($HR3 \sim -0.2$)[10] is consistent with an X-ray absorbed AGN (Della Ceca et al. 2004). This indicates IRAS 14026+4341 as an X-ray absorbed QSO. These objects are often embedded in ultraluminous starburst galaxies (Page et al. 2007), and they have been pointed out as a transitional phase in an evolutionary sequence relating the growth of massive black holes to the formation of galaxies (Stevens et al. 2005; Page et al. 2007).

Under these circumstances, we have selected as best fit the model resulting from fitting the SED without X-ray data. We must note, however, that both models (pure SB or AGN+SB) poorly fit the data between $\sim 1-100\ \mu$m. The observed IR excess, may be related to the X-ray emission absorbed and reprocessed in the IR, can not be reproduced by AGN1 template (an unabsorbed template).

IRAS F15307+3252

This object has been optically classified as a QSO 2 (Rowan-Robinson 2000) and there is strong evidence in X-rays favouring the presence of a heavily obscured AGN (Iwasawa et al. 2005). However we have found that its SED best fit, in terms of χ^2, is obtained with a SB template with minor AGN1 contribution. The CP1 template is also a fair fit, but with a slightly worse χ^2.

Previous analyses of the IR emission of this HLIRG (Deane & Trentham 2001; Verma et al. 2002) suggest that the

---

[10] $HR3 = \frac{CR(2.0-4.5\ {\rm keV})-CR(1.0-2.0\ {\rm keV})}{CR(2.0-4.5\ {\rm keV})+CR(1.0-2.0\ {\rm keV})}$, where CR is the count rate in the given energy band.

SB contribution is considerably lower than what we found using a pure SB template. Hence, we have selected the CP1 as "best fit", which is also consistent with its optical classification, to estimate the AGN and SB contribution to the bolometric luminosity.

6. Comparison with previous results

6.1. X-ray emission

We can estimate the expected X-ray luminosity of the AGN and SB components for each source in our sample using the parameters obtained in our SED analysis, and compare with the X-ray luminosities calculated through XMM-*Newton* observations.

We have seen that the AGN SED of these sources is better modelled with a luminosity-dependent template. Hence, we have employed the relation obtained by Sani et al. (private communication)[11] to estimate the intrinsic 2-10 keV luminosity for a given AGN bolometric luminosity:

$$\frac{L_{2-10\ \mathrm{keV}}}{L_{\mathrm{BOL}}} = 0.043 \left(\frac{L_{\mathrm{BOL}}}{10^{45}}\right)^{-0.357} \tag{2}$$

Figure 7 shows those sources detected in X-rays and with an AGN component in their SED model. We plotted the bolometric luminosity of the AGN component versus the intrinsic (absorption corrected) 2-10 keV luminosity (see Table 3), as calculated in Ruiz et al. (2007).

Most sources are scattered roughly following the Eq. 2 estimate. This scatter is probably related to the intrinsic dispersion in X-ray luminosities of AGN, i.e. for a given bolometric luminosity, there is a broad range of possible X-ray luminosities (Steffen et al. 2006).

There are, however, three sources (PG 1206+459, IRAS F12509+3122 and IRAS 14026+4341) with X-ray luminosities much lower than the estimated by Eq. 2. The X-ray luminosity of IRAS 14026+4341 was calculated using the 2XMMi X-ray fluxes so it is not corrected by absorption. Hence, this large discrepancy between the prediction and the observed luminosity is likely another sign of X-ray absorption (see Sect. 5.4).

For the other two sources Ruiz et al. (2007) did not find any sign of X-ray absorption. This effect could be, in principle, due to an overestimate of the AGN contribution to the bolometric luminosity. If we assume that the difference between the bolometric luminosity calculated using the SED fitting and that estimated using Eq. 2 is completely originated due to star formation, we find that the SB contribution to the total output should be larger than 90% in these two sources. Such a powerful SB must be clearly reflected in the SED shape, but we did not find this kind of deviation in the SED analysis of these sources. The X-ray weakness of these HLIRGs can not therefore be related to the underestimate of the SB contribution to the bolometric output, or due to X-ray absorption. They seem to be intrinsically weak X-ray sources (Leighly et al. 2001, 2007).

6.2. IR SED: comparison with previous work

The IR (1–1000 μm) SED of our sources has been previously studied: Rowan-Robinson (2000), Farrah et al. (2002a) and Verma et al. (2002) modelled it using RTM. We estimated the IR luminosities of our models, integrating between 1–1000 μm, and compared their results with ours (see Table 3).

The IR luminosities estimated through our SED fitting and that estimated using RTM match fairly well (see Fig. 8(a)) for most sources. For three objects, our luminosity estimation is almost an order of magnitude greater than the RTM estimation, probably because our best-fit models overestimate the FIR-submm emission (see Figs. 5(b), 5(f) and 6(f)). This spectral emission is problably better recovered by using RTM. Nevertheless, in spite of this large disagreement in luminosities, our AGN contribution estimates are consistent with those obtained through RTM, as Fig. 8(b) shows.

The latter plot shows that our AGN contribution estimates for most sources are roughly consistent with those obtained through RTM. We can conclude that our simple model based on templates is a fair method to obtain a first estimate of the AGN and SB relative contribution to the IR output.

7. Discussion

The broad band SEDs of the HLIRGs presented in this work can be roughly well fitted using templates, and their best fits are consistent with the optical classification of most sources (9 out of 13). Among class A sources we found three objects fitted with pure type 1 AGN templates. They seem to be very luminous quasars and, since most of their bolometric output is not emitted in the IR band, should not be considered as proper HLIRGs. Four out of seven class A HLIRGs require, in addition to a type 1 AGN template, a SB component which is, in three cases, dominant with respect to the AGN. The AGN emission in four sources is consistent with a luminosity-dependent SED.

On the other hand, we have found that class B sources can not be fitted with simple combination of pure AGN and pure SB templates: a composite template is needed, where AGN and SB phenomena are both significant. This suggests that there should be some feedback between accretion process and star formation that changes the shape of the SED in a way that can not be imitated just by combining a pure SB and a pure AGN components. The main observational imprint of this feedback seems to be an excess in the SED around $\sim 10\ \mu$m with respect to the predicted emission of pure AGN and pure SB combined model.

Our division between class A and class B sources is based on the optical spectral classification, and since all objects show a significant AGN emission, it seems that the SED shape differences between the two groups could be an inclination effect as in the unified model of AGNs (Antonucci & Miller 1985): those HLIRGs where we have a direct view of the nucleus are luminous QSO and show a class A SED, while those HLIRGs seen through the molecular torus and/or other obscuring material show a class B SED. The comparable mean SB contribution of class A (excluding pure AGN sources) and class B sources is consistent with this hypothesis. Within this scenario, all types of HLIRGs belong to the same class of sources, seen at different inclination angles.

Farrah et al. (2002a) proposed, however, that HLIRG population is comprised of (1) mergers between gas rich galaxies, as found in the ULIRG population, and (2) young active galaxies going through their maximal star formation periods whilst harbouring an AGN.

The N_{H} distribution we found in the X-ray study seems to favour the two population hypothesis. In a pure inclination scenario we would expect a broad range of X-ray absorption, from no absorbed to heavily absorbed sources. However we found only objects with no significant intrinsic absorption (all but one class A sources) or CT absorbed objects (all class B sources). Since AGNs observed in ULIRGs usually show heavy absorption in X-rays (Franceschini et al. 2003; Ptak et al. 2003; Teng et al. 2005), in principle class B sources could represent the high luminosity tail of ULIRG population, while the strong SB found in class A HLIRGs could represent young active galaxies experiencing their maximal star formation, without being in interacting systems (i.e. with little connection with a recent major merger).

---

[11] This ratio is obtained from the Steffen et al. (2006) relation between X-ray and 2500 Å luminosities and then linking the 2500 Å luminosity with the bolometric one through the Elvis et al. (1994) SED.

The study of the host galaxy morphology and environment of HLIRGs also support the two population hypothesis. Farrah et al. (2002b) found in a sample of nine HLIRGs observed by HST both strongly interactive systems and objects with no clear signs of ongoing interactions. Five sources of this sample are also included in ours: IRAS F00235+1024 and IRAS F15307+3252 (class B objects) show signs of strong interactions, while IRAS F12509+3122, IRAS F14218+3845 and IRAS 16347+7037 (class A objects) are isolated systems. This result favours our suggestion that class B HLIRGs could be objects in the extreme bright end of the ULIRG population distribution.

Hence, while class B HLIRGs share common properties with ULIRGs (high levels of X-ray obscuration, strong star formation, signs of mergers and interactions), class A HLIRGs seem to be a different class of objects. Excluding the 3 pure AGN sources, class A objects could be among the young active galaxies proposed by Farrah et al. (2002a). The powerful SB we found in these sources, and the large amounts of gas available to fuel the star formation (as calculated by Farrah et al. 2002a), along with the non detection of mergers or interactions in these systems, support this idea. Moreover, the SB emission of the bona fide class A HLIRGs is modelled with young SB templates (SB1 and SB2) in all but one object (IRAS 18216+6418), which is modelled with an old SB (SB3). This source could be a more evolved object.

Therefore, sources in our sample likely belong to three different populations:

1. Very luminous QSO with minor star formation activity.
2. Young, isolated active galaxies undergoing their first episode of major star formation with little connection with a recent major merger.
3. Galaxies which have recently experienced a merger/disturbance that brought lots of gas and dust in the inner regions. This event trigger both the star formation and the AGN activity in a heavily obscured environment. These objects suit well as the high luminosity tail of the ULIRG population.

Nevertheless, our sample of HLIRGs is not complete in any sense and we cannot derive further conclusions about the global properties of the HLIRG population. Further studies established on larger and complete samples of HLIRGs are needed to conclude if the division between class A and class B objects is just due to an inclination effect, or is based on intrinsic differences of their physical properties.

8. Conclusions

In this paper we have built and analysed the multi-wavelength SED (from radio to X-rays) of a sample of 13 HLIRGs, previously studied in detail in X-rays (Ruiz et al. 2007). We assembled the SEDs using public data in several astronomical databases and in the literature, and we modelled them using templates. Most sources are roughly well fitted with this simple model and we find AGN relative contributions consistent with those inferred by previous analyses of the IR SEDs of HLIRGs using radiative transfer models.

We divided the HLIRGs in two groups, accordingly to their optical spectral classification: class A (type 1 AGNs) and class B (type 2 AGNs and SB) sources. A first look at their SED shape indicates some differences between the two classes: class A sources show a roughly flat SED between the IR and the optical, while class B sources have a prominent IR bump dominating the rest of the emission.

A significant fraction (3 out of 7) of class A HLIRGs seem to be very luminous quasars with no particular deviations from the local quasars. Strictly speaking these objects should not be considered HLIRGs since most of their bolometric output is emitted outside the IR band. The SED of these QSO are consistent with a luminosity-dependent quasar template. The remaining class A sources show significant additional SB components, which are dominant in all but one object. Given their strong SB activity and the lack of any sign of mergers in these systems, these HLIRGs could be very young galaxies experiencing their first episode of maximal star formation.

Class B HLIRGs show an IR excess that can not be modelled with any combination of our selected pure AGN and pure SB templates. This feature can be properly fitted using composite templates (SEDs from objects where AGN and SB emission are both important). This suggests that a significant fraction of the emission of this class of objects is originated in a SB. This also shows that the feedback between accretion and star formation processes modifies the SED of class B HLIRGs in a way that can not be replicated by just the addition of pure AGN and pure SB independent templates. Class B HLIRGs share many properties with ULIRGs (high X-ray absorption, strong star formation, signs of mergers and interactions), so they could be just the high luminosity tail of this population.

Therefore, we have found some evidence supporting the idea that bona fide HLIRGs are composed of two populations: young active galaxies with no sign for recent mergers most likely going through their first episode of strong star formation, and the high-luminosity end of the ULIRG population, where both the SB and AGN are likely triggered by a recent merger/interaction. Further observational studies based on larger and, most importantly, complete samples of HLIRGs are needed to obtain stronger evidence for this hypothesis. Moreover our simple template-fitting approach should be complemented with RTMs (or other theoretical models of AGN and SB emission), since the two approaches are complementary in many ways and their combination may shed further light onto the relative SB-AGN contribution and on the feedback processes that take place in the most interesting HLIRGs, namely those that are well represented by composite templates within our approach.

Acknowledgements. We are grateful to the referee M. Rowan-Robinson for the constructive comments and suggestions that improved this paper. A.R. acknowledges support from a Universidad de Cantabria fellowship. Financial support for A.R. and F.J.C. was provided by the Spanish Ministry of Education and Science, under projects ESP2003-00812 and ESP2006-13608-C02-01. FP acknowledges financial support under the project ASI INAF I/08/07/0. GM thanks the Ministerio de Ciencia e Innovación and CSIC for support through a Ramón y Cajal contract.

This research has made use of the NASA/IPAC Extragalactic Database (NED) which is operated by the Jet Propulsion Laboratory, California Institute of Technology, under contract with the National Aeronautics and Space Administration. This paper is based also on data from the VOSED tool at LAEFF.

The 2.5m Isaac Newton Telescope and its service programme are operated on the island of La Palma by the Isaac Newton Group in the Spanish

Observatorio del Roque de los Muchachos of the Instituto de Astrofísica de Canarias.

References

Adelman-McCarthy, J. K., Agüeros, M. A., Allam, S. S., et al. 2007, ApJS, 172, 634

Antonucci, R. R. J. & Miller, J. S. 1985, ApJ, 297, 621

Beck, S. C., Turner, J. L., Ho, P. T. P., Lacy, J. H., & Kelly, D. M. 1996, ApJ, 457, 610

Berta, S. 2005, PhD thesis, AA(Dipartimento di Astronomia, Univ. di Padova, Vicolo dell’Osservatorio 2, I-35122, Padova, Italy)

Berta, S., Fritz, J., Franceschini, A., Bressan, A., & Pernechele, C. 2003, A&A, 403, 119

Bianchi, S., Guainazzi, M., & Chiaberge, M. 2006, A&A, 448, 499

Brandl, B. R., Devost, D., Higdon, S. J. U., et al. 2004, ApJS, 154, 188

Cutri, R. M., Skrutskie, M. F., van Dyk, S., et al. 2003, 2MASS All Sky Catalog of point sources. (The IRSA 2MASS All-Sky Point Source Catalog, NASA/IPAC Infrared Science Archive. http://irsa.ipac.caltech.edu/applications/Gator/)

Davies, R. I., Tacconi, L. J., & Genzel, R. 2004, ApJ, 613, 781

Davis, M., Guhathakurta, P., Konidaris, N. P., et al. 2007, ApJ, 660, L1

Deane, J. R. & Trentham, N. 2001, MNRAS, 326, 1467

Della Ceca, R., Maccacaro, T., Caccianiga, A., et al. 2004, A&A, 428, 383

Dickey, J. M. & Lockman, F. J. 1990, ARA&A, 28, 215

Dickinson, M., Giavalisco, M., & The Goods Team. 2003, in The Mass of Galaxies at Low and High Redshift, ed. R. Bender & A. Renzini, 324

Drake, C. L., Bicknell, G. V., McGregor, P. J., & Dopita, M. A. 2004, AJ, 128, 969

Efstathiou, A. & Rowan-Robinson, M. 1995, MNRAS, 273, 649

Efstathiou, A., Rowan-Robinson, M., & Siebenmorgen, R. 2000, MNRAS, 313, 734

Elvis, M., Wilkes, B. J., McDowell, J. C., et al. 1994, ApJS, 95, 1

Fabian, A. C. & Iwasawa, K. 1999, MNRAS, 303, L34

Farrah, D., Afonso, J., Efstathiou, A., et al. 2003, MNRAS, 343, 585

Farrah, D., Rowan-Robinson, M., Oliver, S., et al. 2001, MNRAS, 326, 1333

Farrah, D., Serjeant, S., Efstathiou, A., Rowan-Robinson, M., & Verma, A. 2002a, MNRAS, 335, 1163

Farrah, D., Verma, A., Oliver, S., Rowan-Robinson, M., & McMahon, R. 2002b, MNRAS, 329, 605

Franceschini, A., Braito, V., Persic, M., et al. 2003, MNRAS, 343, 1181

Franceschini, A., Hasinger, G., Miyaji, T., & Malquori, D. 1999, MNRAS, 310, L5

Freeman, P., Doe, S., & Siemiginowska, A. 2001, in Presented at the Society of Photo-Optical Instrumentation Engineers (SPIE) Conference, Vol. 4477, Society of Photo-Optical Instrumentation Engineers (SPIE) Conference Series, ed. J.-L. Starck & F. D. Murtagh, 76–87

Gilli, R., Comastri, A., & Hasinger, G. 2007, A&A, 463, 79

Gonzalez-Delgado, R. M., Perez, E., Diaz, A. I., et al. 1995, ApJ, 439, 604

Hopkins, P. F., Richards, G. T., & Hernquist, L. 2007, ApJ, 654, 731

Imanishi, M., Dudley, C. C., Maiolino, R., et al. 2007, ApJS, 171, 72

Iwasawa, K., Crawford, C. S., Fabian, A. C., & Wilman, R. J. 2005, MNRAS, 362, L20

Joint IRAS Science Working Group. 1988, in IRAS Point Source Catalog (1988)

Kelly, B. C., Bechtold, J., Trump, J. R., Vestergaard, M., & Siemiginowska, A. 2008, ApJS, 176, 355

Kleinmann, S. G., Hamilton, D., Keel, W. C., et al. 1988, ApJ, 328, 161

Kormendy, J. & Gebhardt, K. 2001, in American Institute of Physics Conference Series, Vol. 586, 20th Texas Symposium on relativistic astrophysics, ed. J. C. Wheeler & H. Martel, 363

Leighly, K. M., Halpern, J. P., Helfand, D. J., Becker, R. H., & Impey, C. D. 2001, AJ, 121, 2889

Leighly, K. M., Halpern, J. P., Jenkins, E. B., et al. 2007, ApJ, 663, 103

Lonsdale, C. J., Farrah, D., & Smith, H. E. 2006, Ultraluminous Infrared Galaxies, ed. J. W. Mason (Springer Verlag), 285

Magdziarz, P. & Zdziarski, A. A. 1995, MNRAS, 273, 837

Magorrian, J., Tremaine, S., Richstone, D., et al. 1998, AJ, 115, 2285

Matt, G., Guainazzi, M., Frontera, F., et al. 1997, A&A, 325, L13

McLure, R. J. & Dunlop, J. S. 2002, MNRAS, 331, 795

Moshir, M., Kopan, G., Conrow, T., et al. 1990, in IRAS Faint Source Catalogue, version 2.0 (1990)

Nardini, E., Risaliti, G., Salvati, M., et al. 2008, MNRAS, 385, L130

Neugebauer, G., Green, R. F., Matthews, K., et al. 1987, ApJS, 63, 615

Page, M. J., Carrera, F. J., Ebrero, J., Stevens, J. A., & Ivison, R. J. 2007, in Studying Galaxy Evolution with Spitzer and Herschel, ed. V. Charmandaris, D. Rigopoulou, & N. Kylafis

Persic, M. & Rephaeli, Y. 2002, A&A, 382, 843

Ptak, A., Heckman, T., Levenson, N. A., Weaver, K., & Strickland, D. 2003, ApJ, 592, 782

Quinn, P. J., Barnes, D. G., Csabai, I., et al. 2004, in Presented at the Society of Photo-Optical Instrumentation Engineers (SPIE) Conference, Vol. 5493, Society of Photo-Optical Instrumentation Engineers (SPIE) Conference Series, ed. P. J. Quinn & A. Bridger, 137–145

Richards, G. T., Lacy, M., Storrie-Lombardi, L. J., et al. 2006, ApJS, 166, 470

Risaliti, G. & Elvis, M. 2004, A Panchromatic View of AGN (ASSL Vol. 308: Supermassive Black Holes in the Distant Universe), 187

Rowan-Robinson, M. 1995, MNRAS, 272, 737

Rowan-Robinson, M. 2000, MNRAS, 316, 885

Ruiz, A., Carrera, F. J., & Panessa, F. 2007, A&A, 471, 775

Scoville, N., Aussel, H., Brusa, M., et al. 2007, ApJS, 172, 1

Silverman, J. D., Green, P. J., Barkhouse, W. A., et al. 2005, ApJ, 624, 630

Spergel, D. N., Verde, L., Peiris, H. V., et al. 2003, ApJS, 148, 175

Steffen, A. T., Strateva, I., Brandt, W. N., et al. 2006, AJ, 131, 2826

Stevens, J. A., Page, M. J., Ivison, R. J., et al. 2005, MNRAS, 360, 610

Strateva, I. V., Brandt, W. N., Schneider, D. P., Vanden Berk, D. G., & Vignali, C. 2005, AJ, 130, 387

Strickland, D. K., Heckman, T. M., Colbert, E. J. M., Hoopes, C. G., & Weaver, K. A. 2004, ApJS, 151, 193

Telesco, C. M., Becklin, E. E., Wynn-Williams, C. G., & Harper, D. A. 1984, ApJ, 282, 427

Teng, S. H., Wilson, A. S., Veilleux, S., et al. 2005, ApJ, 633, 664

Ueda, Y., Akiyama, M., Ohta, K., & Miyaji, T. 2003, ApJ, 598, 886

Veilleux, S., Kim, D.-C., & Sanders, D. B. 1999, ApJ, 522, 113

Veilleux, S., Kim, D.-C., & Sanders, D. B. 2002, ApJS, 143, 315

Veilleux, S., Kim, D.-C., Sanders, D. B., Mazzarella, J. M., & Soifer, B. T. 1995, ApJS, 98, 171

Verma, A., Rowan-Robinson, M., McMahon, R., & Andreas Efstathiou, A. E. 2002, MNRAS, 335, 574

Watson, M. G., Schröder, A. C., Fyfe, D., et al. 2009, A&A, 493, 339

Wilman, R. J., Fabian, A. C., Crawford, C. S., & Cutri, R. M. 2003, MNRAS, 338, L19

Wilman, R. J., Fabian, A. C., Cutri, R. M., Crawford, C. S., & Brandt, W. N. 1998, MNRAS, 300, L7

Table 1. Best fit models for the HLIRG's SEDs

Source	z	Type	CT[a]	Best Fit model[b]							log L_{BOL} [c] (erg s^{-1})	AGN / SB[d]
				all data[e]			no X-rays[f]			composite temp.[g]		
				Model		α	Model		α			
Class A HLIRGs												
PG 1206+459	1.158	QSO	N	AGN1-L	...	1	AGN1	...	1	**AGN1-L**	48.4	1 / 0
PG 1247+267	2.038	QSO	N	AGN1-L	...	1	AGN1	...	1	**AGN1-L**	49.2	1 / 0
IRAS F12509+3122	0.780	QSO	N	AGN1-L	SB1	0.3	AGN1	SB4	0.5	**AGN1-L+SB1**	47.7	0.3 / 0.7
IRAS 14026+4341	0.323	QSO	N	...	SB2	0	**AGN1**	**SB2**	0.3	SB2	46.7	0.3 / 0.7
IRAS F14218+3845	1.21	QSO	N	AGN1	SB1	0.4	AGN1	SB1	0.3	**AGN1+SB1**	47.2	0.4 / 0.6
IRAS 16347+7037	1.334	QSO	N	AGN1-L	...	1	AGN1	...	1	**AGN1-L**	48.9	1 / 0
IRAS 18216+6418	0.297	QSO	N	AGN1	SB3	0.8	AGN1	SB3	0.8	**AGN1+SB3**	47.4	0.8 / 0.2
Class B HLIRGs												
IRAS F00235+1024	0.575	NL-SB	Y	...	SB3	0	...	SB3	0	**CP1**	46.7	~0.5 / ~0.5
IRAS 07380-2342	0.292	SB	N	AGN4	SB1	0.06	AGN3	SB1	0.3	**CP1**	47.0	~0.5 / ~0.5
IRAS 00182-7112	0.327	QSO 2	Y	AGN3	SB4	0.06	AGN3	SB3	0.3	**CP1**	46.6	~0.5 / ~0.5
IRAS 09104+4109	0.442	QSO 2	Y	AGN4	SB4	0.09	AGN3	SB1	0.8	**CP2**	47.3	~0.7 / ~0.3
IRAS 12514+1027	0.32	Sy2	Y	AGN5	SB4	0.06	AGN3	SB2	0.9	**CP2**	46.7	~0.7 / ~0.3
IRAS F15307+3252	0.926	QSO 2	Y	AGN1	SB3	0.03	AGN3	SB1	0.8	**CP1**	47.9	~0.5 / ~0.5

[a] Compton Thick candidates.
[b] The best fit adopted to estimate the bolometric luminosity and the AGN and SB fraction is marked in bold fonts.
[c] Bolometric luminosity in CGS units.
[d] Fraction of the bolometric luminosity originated in AGN and SB. Calculated through the parameter α of the best fit model.
[e] Best fit using our original set of templates.
[f] Best fit not using X-ray data.
[g] Best fit including the templates of composite sources.

Table 2. SED templates used as models.

Label	Source	Description
AGN1	...	local quasar's mean SED[1]
AGN1-L	...	luminosity-dependent QSO SED[2]
AGN3	NGC 5506	Sy2, $N_{\mathrm{H}} = 3 \times 10^{22}\mathrm{cm}^{-2}$
AGN4	NGC 4507	Sy2, $N_{\mathrm{H}} = 4 \times 10^{23}\mathrm{cm}^{-2}$
AGN5	Mnk 3	Sy2, $N_{\mathrm{H}} = 1.4 \times 10^{24}\mathrm{cm}^{-2}$
AGN6	NGC 3393	Sy2, $N_{\mathrm{H}} > 1 \times 10^{25}\mathrm{cm}^{-2}$
SB1	NGC 5253	Young and dusty SB
SB2	NGC 7714	Young and unobscured SB
SB3	M82	Old SB
SB4	IRAS 12112+0305	ULIRG
CP1	NGC1068	Composite template: AGN: ~ 50%
CP2	Mnk 231	Composite template: AGN: ~ 70%
CP3	IRAS 19254-7245	Composite template: AGN: ~ 45%
CP4	IRAS 22491-1808	Composite template: AGN: ~ 70%

References. (1) Richards et al. 2006; (2) Hopkins et al. 2007.

Table 3. IR and X-ray luminosities.

Source	$\log L_{\rm IR}^{\rm tot}$ [a] (erg s^{-1})	$\log L_{\rm IR}^{\rm AGN}$ [a] (erg s^{-1})	$\log L_{\rm IR}^{\rm SB}$ [a] (erg s^{-1})	$\log L_{\rm IR,RTM}^{\rm tot}$ [b] (erg s^{-1})	$\log L_{\rm IR,RTM}^{\rm AGN}$ [b] (erg s^{-1})	$\log L_{\rm IR,RTM}^{\rm SB}$ [b] (erg s^{-1})	$\log L_{\rm X}^{\rm AGN}$ [c] (erg s^{-1})	$N_{\rm H}$ [d] (cm^{-2})
Class A HLIRGs								
PG 1206+459	48.0	48.0	0	47.8	47.8	< 46.7	$45.11^{+0.02}_{-0.04}$	...
PG 1247+267	48.8	48.8	0	47.9	47.9	< 46.8	$45.93^{+0.02}_{-0.03}$	...
IRAS F12509+3122	47.6	46.8	47.5	47.0	46.8	46.6	$42.26^{+0.05}_{-0.05}$	...
IRAS 14026+4341[e]	46.5	45.8	46.5	46.5	46.3	46.1	$42.7^{+0.2}_{-0.5}$	...
IRAS F14218+3845	47.1	46.5	46.9	46.9	46.1	46.8	$44.60^{+0.03}_{-0.03}$	...
IRAS 16347+7037	48.5	48.5	0	47.7	47.7	< 46.8	$46.00^{+0.07}_{-0.09}$	...
IRAS 18216+6418	47.1	46.9	46.6	46.8	46.6	46.4	$45.6^{+0.04}_{-0.05}$	...
Class B HLIRGs								
IRAS F00235+1024	46.7	46.4	46.4	46.7	46.4	46.4	< 42.2	$> 10^{25}$
IRAS 07380-2342	47.0	46.7	46.7	47.0	46.8	46.5	< 41.7	...
IRAS 00182-7112	46.6	46.3	46.3	46.7	< 46.5	46.7	$44.82^{+0.16}_{-0.14}$	$> 10^{25}$
IRAS 09104+4109	47.3	47.1	46.8	46.8	46.8	< 46.2	$45.30^{+0.36}_{-0.09}$	$> 10^{25}$
IRAS 12514+1027	46.7	46.5	46.2	46.5	46.2	46.2	$43.3^{+1.4}_{-0.7}$	$(4^{+20}_{-3}) \times 10^{23}$
IRAS F15307+3252	47.9	47.6	47.6	46.9	46.6	46.7	$45.49^{+0.09}_{-0.11}$	$> 10^{25}$

a) IR luminosities (1-1000 μm) estimated using our SED fitting.
b) IR luminosities (1-1000 μm) estimated by the analysis of the IR SED using RTM (Rowan-Robinson 2000; Farrah et al. 2002a).
c) Absorption corrected 2-10 keV luminosities from Ruiz et al. (2007).
d) Intrinsic absorption estimated using X-ray spectra (Ruiz et al. 2007).
e) The X-ray luminosity of this source has been calculated from 2XMMi fluxes (Watson et al. 2009), and it is not corrected from absorption.

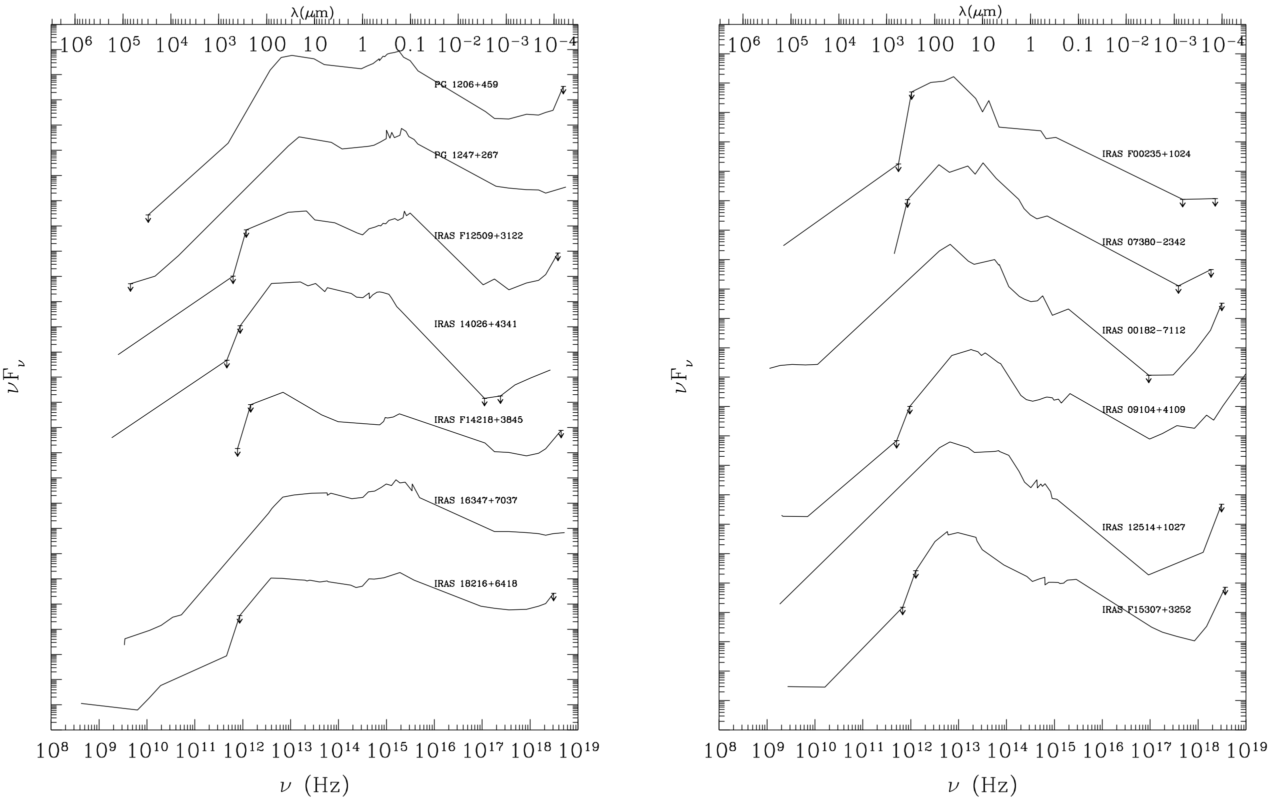

(a) Class A HLIRGs.

(b) Class B HLIRGs.

Fig. 1. Rest-frame spectral energy distributions of the sample. Fluxes are shifted for clarity.

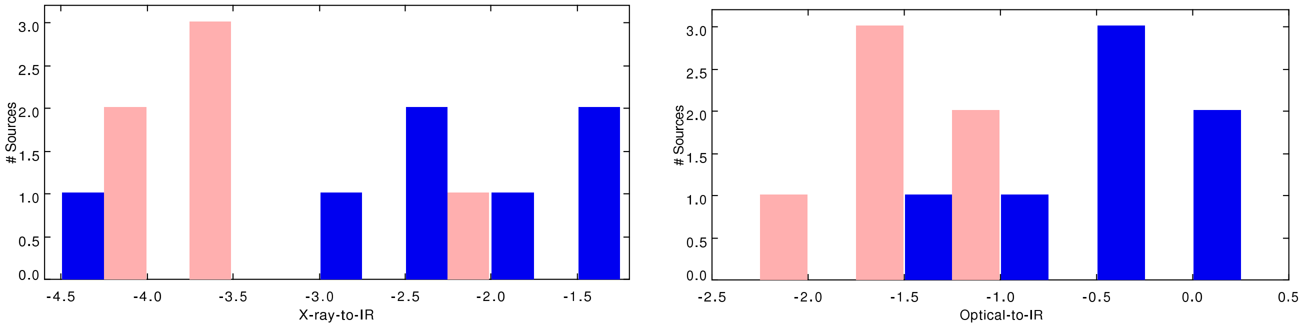

(a) $F_{\rm X}/F_{\rm IR}$ (b) $F_{\rm opt}/F_{\rm IR}$

Fig. 2. Distribution of (a) X-ray-to-IR and (b) Optical-to-IR flux ratios for class A (dark grey, blue in the colour version) and class B (light grey, pink in the colour version) HLIRGs.

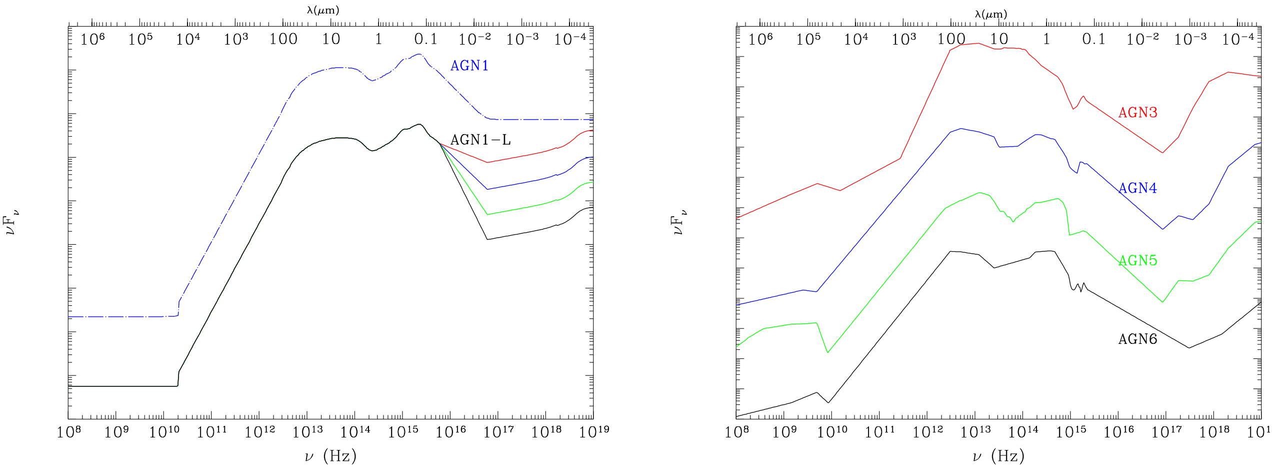

(a) AGN I templates. (b) AGN II templates.

Fig. 3. AGN templates. (a) The top line (blue in the colour version) is the standard SED for radio quiet quasar (AGN1, Richards et al. 2006). The group below is the luminosity-dependent SED for quasar (AGN1-L, Hopkins et al. 2007), plotted for several bolometric luminosities (the top line - red in the colour version - is for $10^{10}\ L_{\odot}$ and the bottom black line is for $10^{16}\ L_{\odot}$). (b) Listed downwards: NGC 5506 (AGN3, $N_{\rm H} = 3\times10^{22}{\rm cm}^{-2}$), NGC 4507 (AGN4, $N_{\rm H} = 4\times10^{23}{\rm cm}^{-2}$), Mrk 3 (AGN5, $N_{\rm H} = 1.4\times10^{24}{\rm cm}^{-2}$), NGC 3393 (AGN6, $N_{\rm H} > 1\times10^{25}{\rm cm}^{-2}$). The SED fluxes are shifted for clarity. See Sect. 4.1 for details.

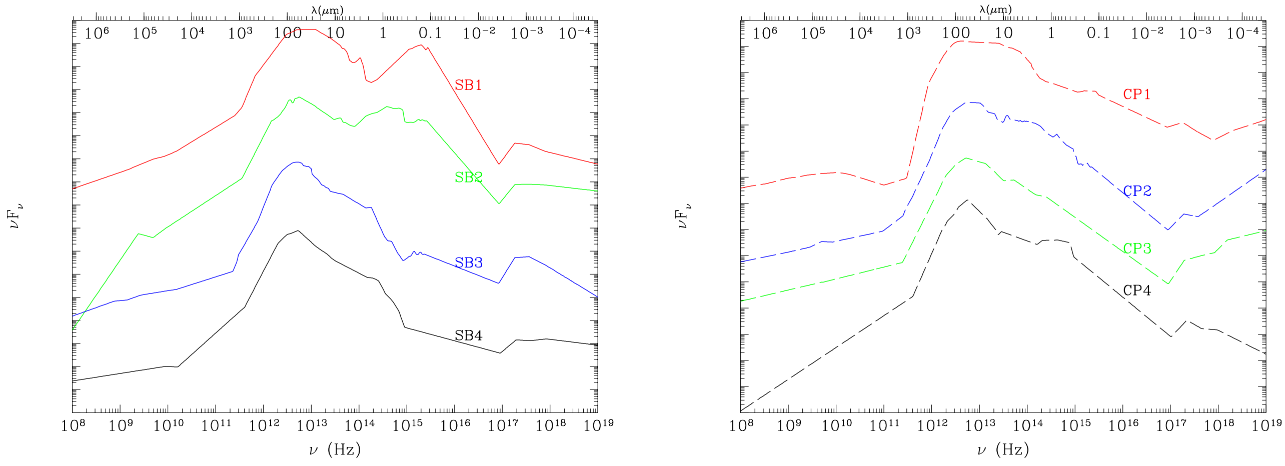

(a) SB templates. (b) Composite templates.

Fig. 4. (a) Pure starburst templates. Listed downwards: NGC 5253, NGC 7714, M82, IRAS 12112+0305. (b) Composite templates (AGN + SB). Listed downwards: NGC 1068, Mrk 231, IRAS 19254-7245, IRAS 22491-1808. The SED fluxes are shifted for clarity. See Sect. 4.1 for details.

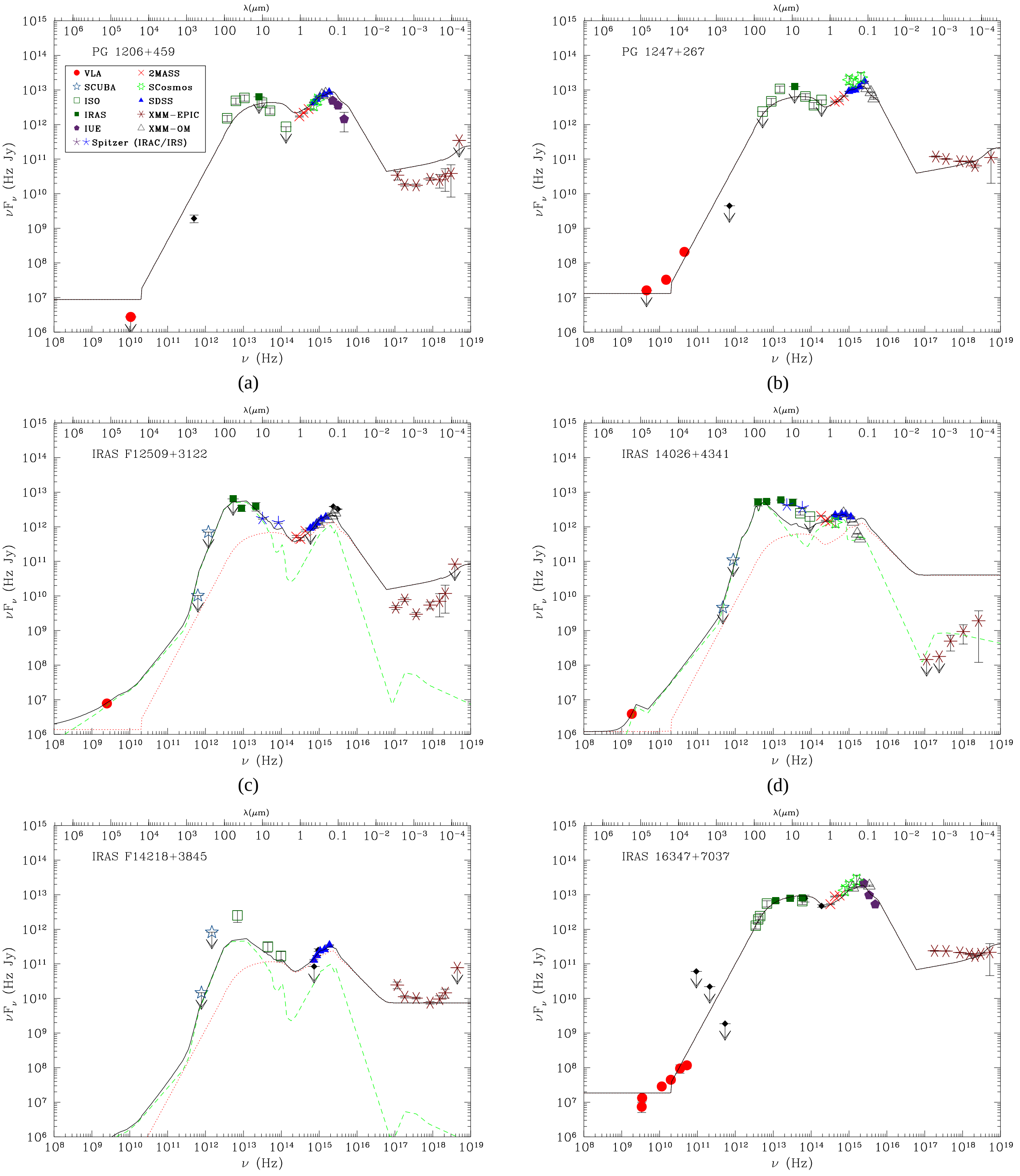

(a) (b)

(c) (d)

(e) (f)

Fig. 5. Rest-frame Spectral Energy Distributions of class A HLIRGs and their best fit models. Dotted lines (red in the colour version) are the AGN components and dashed lines (green in the colour version) are the SB components. Black solid lines are the sum of the AGN and SB components.

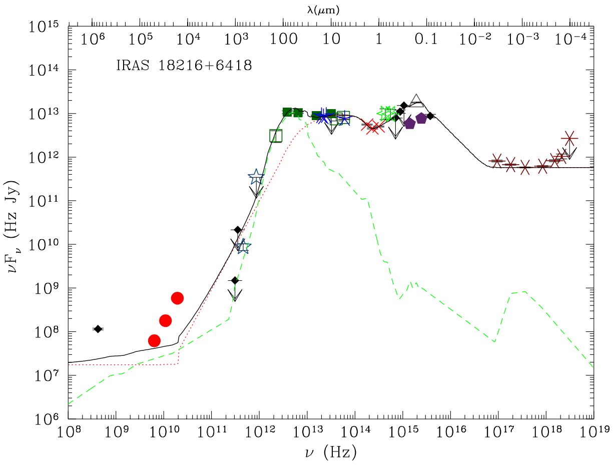

(g)

Fig. 5. Continued.

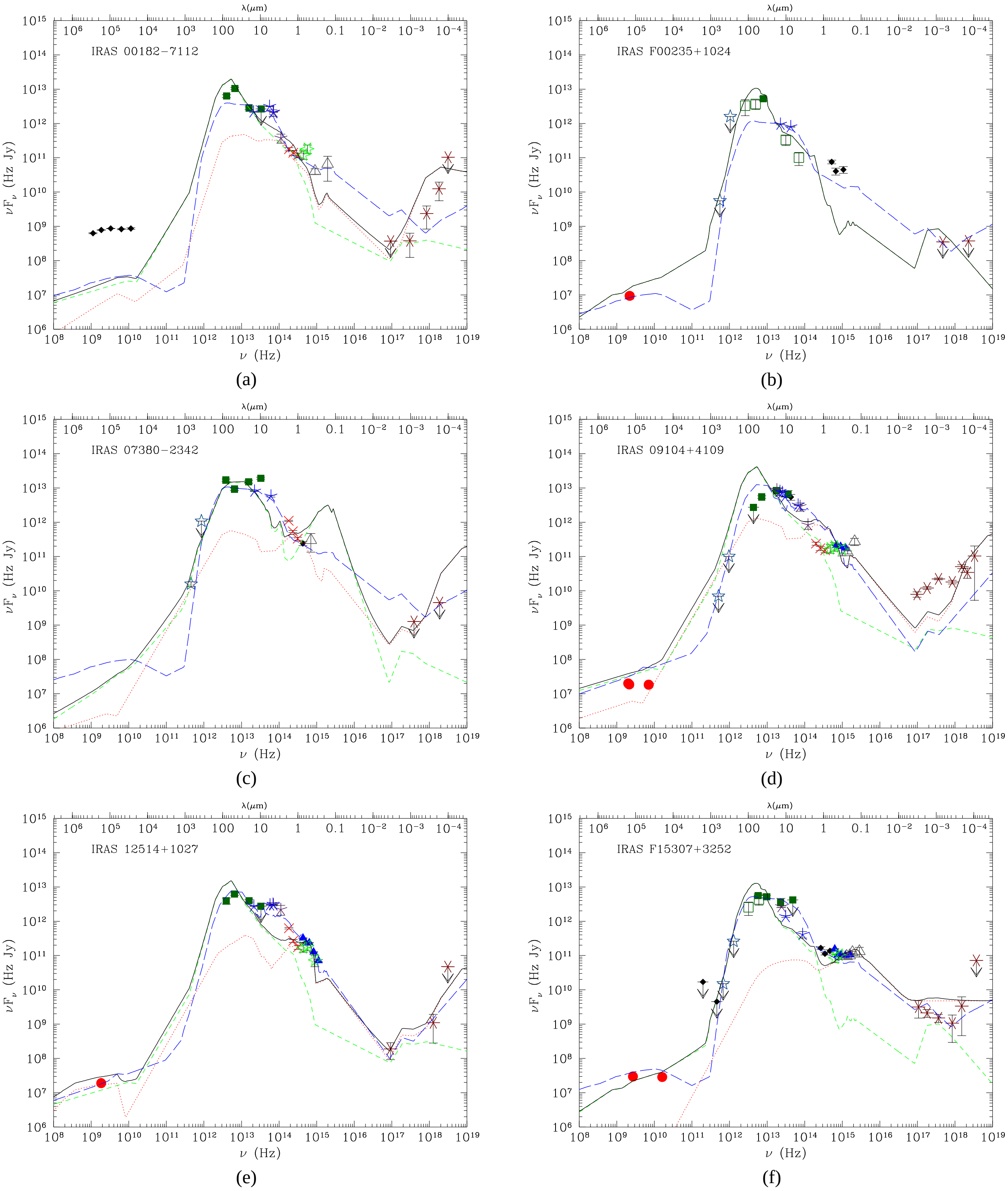

(a) (b) (c) (d) (e) (f)

Fig. 6. Rest-frame Spectral Energy Distributions of class B HLIRGs and their best fit models. Symbols as in Fig. 5. The long-dashed lines (blue in the colour version) are the best fits obtained using composite templates (see Sects. 4.1 and 5.2).

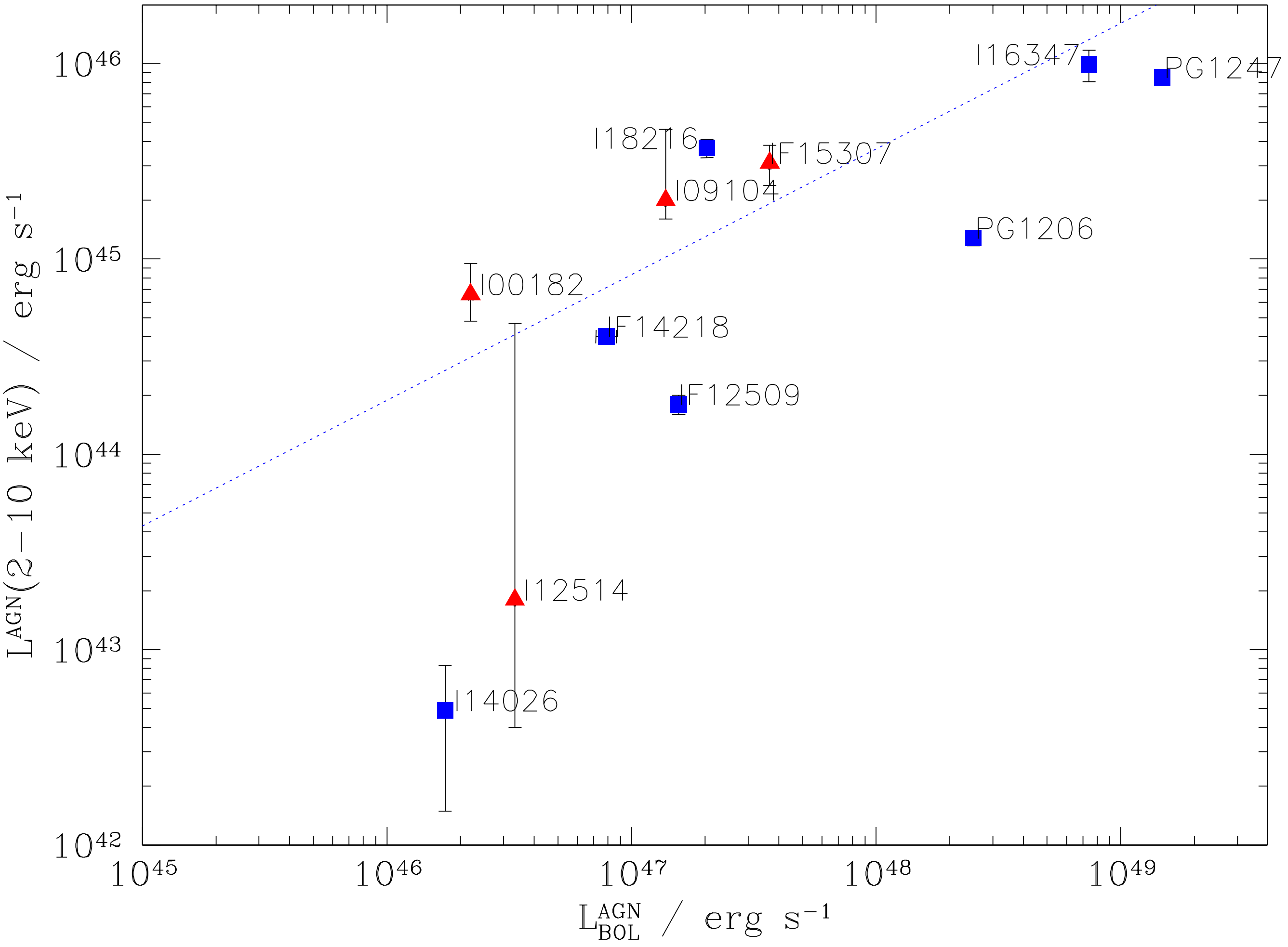

Fig. 7. Bolometric versus observed, absorption-corrected 2-10 keV AGN luminosities. Squares (blue in the colour version) are class A HLIRGs, triangles (red in the colour version) are class B HLIRGs. The dotted line reflects the ratio between these luminosities obtained by Sani et al.

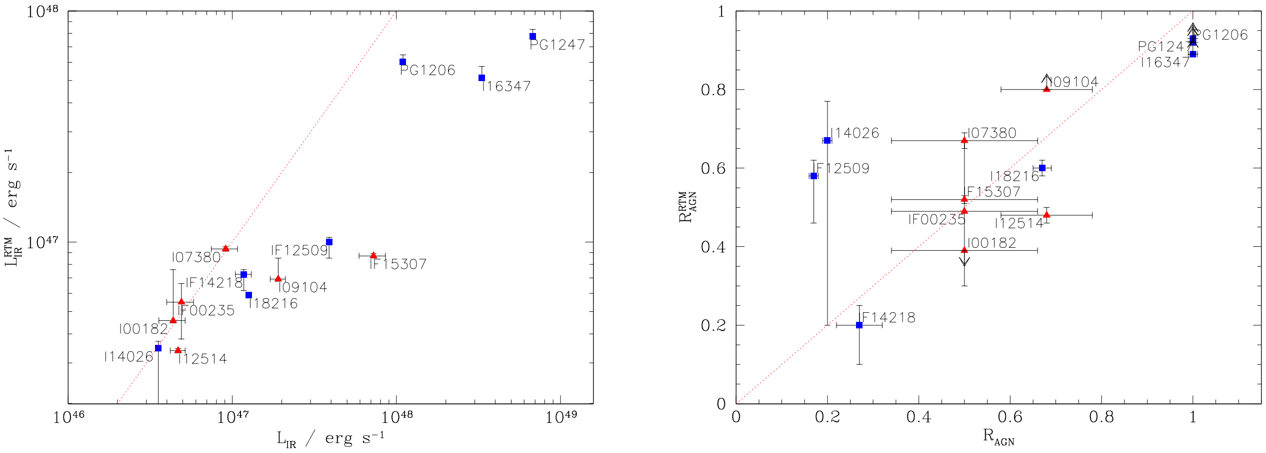

(a) Total IR luminosities.

(b) AGN to total IR luminosity ratios.

Fig. 8. (a) Total IR luminosity estimated using our templates (L_{IR}) and using radiative transfer models (L^{RTM}_{IR}). (b) AGN to total IR luminosity ratios estimated through our model (R_{AGN}) and using radiative transfer models (R^{RTM}_{AGN}). Symbols as in Fig. 7. The dotted lines mean equal values.

Appendix A: IRAS 13279+3401

The object IRAS 13279+3401 has been previously classified as a QSO, and the IR luminosity estimated through the redshift presented in the literature (z=0.36, Rowan-Robinson 2000; Farrah et al. 2002a) exceed the HLIRG limit. However, we have now strong evidence showing that this source is a much closer galaxy.

Figure A.1(a) shows its optical spectrum obtained by the 2.5m Isaac Newton Telescope, where we do not find any type I feature. A QSO with z=0.36 should present a broad H_β emission line at $\sim$ 6600 Å. We estimate z=0.023 for this spectrum, from stellar absorption features.

We have also the MIR spectrum of this source, observed by *Spitzer* (see Fig. A.1(b)). We have estimated the redshift of the source using a SB template from Nardini et al. (2008). We redshifted the template matching the most important spectral features and we found $z \sim 0.02$, which is consistent with our estimate using the optical spectrum. The IR luminosity derived from this redshift is $\sim 3 \times 10^{10}\ L_\odot$, well below the HLIRG limit and even below the LIRG.

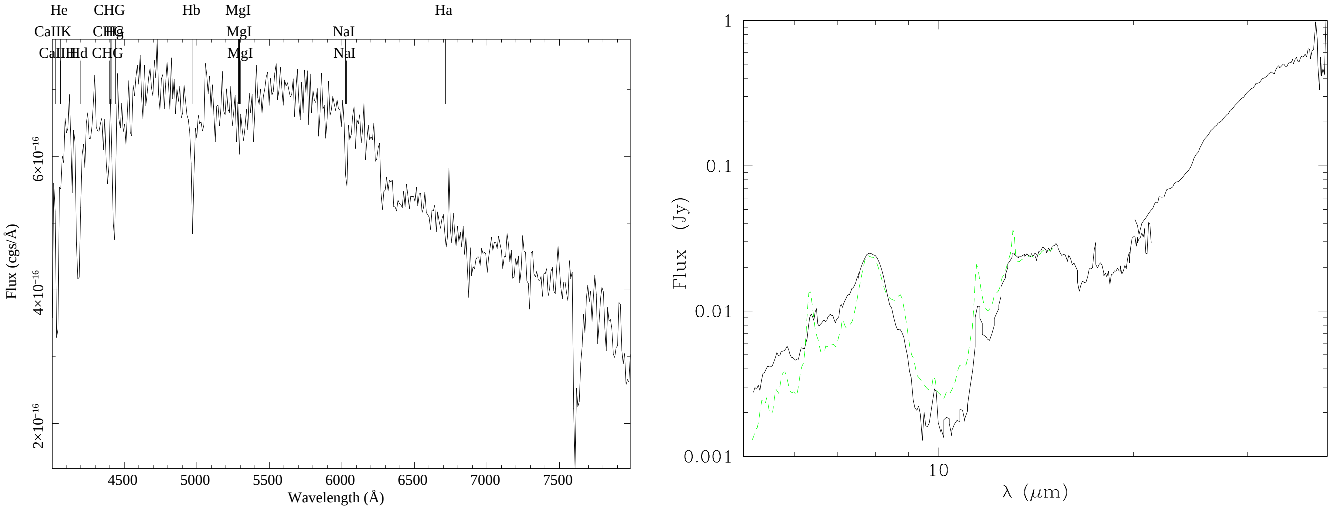

(a) Optical spectrum (2.5m INT).

(b) MIR spectrum (*Spitzer* Infrared Spectrograph).

Fig. A.1. (a) Optical and (b) MIR spectra of IRAS 13279+3401 in the observer frame. The slashed line (green in the colour version) in the right hand side plot is the SB template from Nardini et al. (2008).

Appendix B: Tables of data

Along this appendix a table is presented for each object with the fluxes employed to build the SEDs and the origin of each data. The re-binned spectra from XMM-*Newton* and *Spitzer* are not included in these tables. Fluxes shown with no errors are upper limits.

Table B.1. Photometric data for IRAS 00182-7112.

ν (Hz)	F_ν (Jy)	Error (Jy)	Ref.
8.43×10^{8}	4.23×10^{-1}	1.28×10^{-2}	SUMSS (NED)
1.40×10^{9}	3.17×10^{-1}	3.00×10^{-3}	ATCA (Drake et al. 2004)
2.50×10^{9}	1.97×10^{-1}	3.00×10^{-3}	ATCA (Drake et al. 2004)
4.80×10^{9}	9.80×10^{-2}	3.00×10^{-3}	ATCA (Drake et al. 2004)
8.60×10^{9}	5.70×10^{-2}	3.00×10^{-3}	ATCA (Drake et al. 2004)
3.00×10^{12}	1.19×10^{0}	1.19×10^{-1}	IRAS (NED)
5.00×10^{12}	1.20×10^{0}	8.37×10^{-2}	IRAS (NED)
1.20×10^{13}	1.33×10^{-1}	1.02×10^{-2}	IRAS (NED)
2.50×10^{13}	6.02×10^{-2}	...	IRAS (NED)
5.23×10^{13}	2.23×10^{-2}	4.78×10^{-3}	*Spitzer* -IRAC
8.44×10^{13}	2.53×10^{-3}	7.47×10^{-4}	*Spitzer* -IRAC
1.39×10^{14}	7.22×10^{-4}	7.83×10^{-5}	2MASS
1.80×10^{14}	4.37×10^{-4}	7.34×10^{-5}	2MASS
2.43×10^{14}	2.68×10^{-4}	4.34×10^{-5}	2MASS
3.33×10^{14}	2.02×10^{-4}	5.57×10^{-5}	SSS
4.28×10^{14}	2.28×10^{-4}	6.30×10^{-5}	SSS
6.81×10^{14}	2.97×10^{-5}	5.40×10^{-6}	XMM-*Newton* -OM
1.48×10^{15}	1.90×10^{-5}	1.30×10^{-5}	XMM-*Newton* -OM

Table B.2. Photometric data for IRAS F00235+1024.

ν (Hz)	F_ν (Jy)	Error (Jy)	Ref.
1.40×10^{9}	2.70×10^{-3}	5.00×10^{-4}	VLA (NED)
3.53×10^{11}	6.38×10^{-3}	...	SCUBA (Farrah et al. 2002a)
6.66×10^{11}	9.67×10^{-1}	...	SCUBA (Farrah et al. 2002a)
1.66×10^{12}	8.05×10^{-1}	3.93×10^{-1}	ISO (NED)
3.15×10^{12}	4.78×10^{-1}	1.48×10^{-1}	ISO (NED)
5.00×10^{12}	4.28×10^{-1}	5.56×10^{-2}	IRAS (NED)
2.00×10^{13}	6.75×10^{-3}	2.14×10^{-3}	ISO (NED)
4.44×10^{13}	9.20×10^{-4}	3.80×10^{-4}	ISO (NED)
1.39×10^{14}	1.01×10^{-4}	5.00×10^{-6}	(Farrah et al. 2002a)
3.33×10^{14}	8.00×10^{-5}	1.00×10^{-5}	(Farrah et al. 2002a)
4.28×10^{14}	3.10×10^{-5}	7.00×10^{-6}	USNO-B1.0
6.81×10^{14}	1.80×10^{-5}	4.00×10^{-6}	USNO-B1.0
3.02×10^{17}	4.68×10^{-10}	...	XMM-*Newton* -EPIC
1.45×10^{18}	1.04×10^{-10}	...	XMM-*Newton* -EPIC

Table B.3. Photometric data for IRAS 07380-2342.

ν (Hz)	F_ν (Jy)	Error (Jy)	Ref.
3.53×10^{11}	2.68×10^{-2}	4.20×10^{-3}	SCUBA (Farrah et al. 2002a)
6.66×10^{11}	9.67×10^{-1}	...	SCUBA (Farrah et al. 2002a)
3.00×10^{12}	3.55×10^{0}	2.84×10^{-1}	IRAS (NED)
5.00×10^{12}	1.17×10^{0}	9.36×10^{-2}	IRAS (NED)
1.20×10^{13}	8.00×10^{-1}	8.00×10^{-2}	IRAS (NED)
2.50×10^{13}	4.84×10^{-1}	3.39×10^{-2}	IRAS (NED)
1.39×10^{14}	4.08×10^{-3}	1.49×10^{-4}	2MASS
1.80×10^{14}	1.35×10^{-3}	9.71×10^{-5}	2MASS
2.43×10^{14}	4.74×10^{-4}	4.79×10^{-5}	2MASS
3.33×10^{14}	1.62×10^{-4}	2.23×10^{-5}	DENIS
5.45×10^{14}	3.80×10^{-5}	2.10×10^{-5}	XMM-*Newton* -OM
3.02×10^{17}	2.51×10^{-9}	...	XMM-*Newton* -EPIC
1.45×10^{18}	1.87×10^{-9}	...	XMM-*Newton* -EPIC

Table B.4. Photometric data for IRAS 09104+4109.

ν (Hz)	F_ν (Jy)	Error (Jy)	Ref.
1.40×10^{9}	6.88×10^{-3}	1.31×10^{-4}	VLA (NED)
1.49×10^{9}	6.00×10^{-3}	1.00×10^{-3}	VLA (NED)
4.90×10^{9}	1.80×10^{-3}	3.00×10^{-4}	VLA (NED)
3.53×10^{11}	9.54×10^{-3}	...	SCUBA (Farrah et al. 2002a)
6.66×10^{11}	7.28×10^{-2}	...	SCUBA (Farrah et al. 2002a)
3.00×10^{12}	4.38×10^{-1}	...	IRAS (NED)
5.00×10^{12}	5.25×10^{-1}	4.20×10^{-2}	IRAS (NED)
1.20×10^{13}	3.34×10^{-1}	1.30×10^{-2}	IRAS (NED)
1.26×10^{13}	3.33×10^{-1}	1.70×10^{-2}	*Spitzer* -IRAC
1.43×10^{13}	2.70×10^{-1}	7.00×10^{-2}	IRTF (Kleinmann et al. 1988)
2.50×10^{13}	1.30×10^{-1}	3.11×10^{-2}	IRAS (NED)
2.97×10^{13}	8.80×10^{-2}	1.70×10^{-2}	IRTF (Kleinmann et al. 1988)
5.23×10^{13}	2.64×10^{-2}	7.11×10^{-3}	*Spitzer* -IRAC
8.44×10^{13}	4.74×10^{-3}	1.21×10^{-3}	*Spitzer* -IRAC
1.39×10^{14}	8.21×10^{-4}	8.61×10^{-5}	2MASS
1.80×10^{14}	4.59×10^{-4}	6.24×10^{-5}	2MASS
2.43×10^{14}	2.97×10^{-4}	4.64×10^{-5}	2MASS
3.33×10^{14}	2.42×10^{-4}	6.69×10^{-5}	SSS
3.28×10^{14}	5.06×10^{-4}	7.45×10^{-6}	SDSS-DR5
3.93×10^{14}	7.04×10^{-4}	3.42×10^{-6}	SDSS-DR5
4.28×10^{14}	2.12×10^{-4}	5.85×10^{-5}	SSS
4.81×10^{14}	2.11×10^{-4}	1.69×10^{-6}	SDSS-DR5
6.28×10^{14}	1.51×10^{-4}	1.26×10^{-6}	SDSS-DR5
6.81×10^{14}	1.08×10^{-4}	3.97×10^{-5}	SSS
8.47×10^{14}	1.01×10^{-4}	3.16×10^{-6}	SDSS-DR5
9.67×10^{14}	5.90×10^{-5}	6.00×10^{-6}	XMM-*Newton* -OM
1.48×10^{15}	7.50×10^{-5}	1.80×10^{-5}	XMM-*Newton* -OM
7.86×10^{18}	1.06×10^{-7}	5.91×10^{-8}	BeppoSAX (NED)

Table B.5. Photometric data for PG 1206+459.

ν (Hz)	F_ν (Jy)	Error (Jy)	Ref.
4.90×10^{9}	1.20×10^{-4}	...	VLA (NED)
2.30×10^{11}	1.80×10^{-3}	4.50×10^{-4}	IRAM (NED)
1.72×10^{12}	1.89×10^{-1}	3.78×10^{-2}	ISO (NED)
2.93×10^{12}	3.53×10^{-1}	7.06×10^{-2}	ISO (NED)
4.93×10^{12}	2.57×10^{-1}	5.14×10^{-2}	ISO (NED)
1.20×10^{13}	1.13×10^{-1}	...	IRAS (NED)
1.43×10^{13}	6.40×10^{-2}	1.28×10^{-2}	ISO (NED)
2.34×10^{13}	2.30×10^{-2}	4.60×10^{-3}	ISO (NED)
2.50×10^{13}	2.07×10^{-1}	3.60×10^{-2}	IRAS (NED)
6.17×10^{13}	3.00×10^{-3}	...	ISO (NED)
1.39×10^{14}	2.64×10^{-3}	9.46×10^{-5}	2MASS
1.80×10^{14}	2.57×10^{-3}	1.22×10^{-4}	2MASS
2.43×10^{14}	2.43×10^{-3}	7.76×10^{-5}	2MASS
3.33×10^{14}	2.27×10^{-3}	6.26×10^{-4}	SSS
3.28×10^{14}	2.78×10^{-3}	1.26×10^{-5}	SDSS-DR5
3.93×10^{14}	2.94×10^{-3}	9.76×10^{-6}	SDSS-DR5
4.28×10^{14}	2.51×10^{-3}	6.93×10^{-4}	SSS
4.81×10^{14}	2.92×10^{-3}	9.45×10^{-6}	SDSS-DR5
5.45×10^{14}	2.62×10^{-3}	3.00×10^{-5}	XMM-*Newton* -OM
6.28×10^{14}	2.53×10^{-3}	7.01×10^{-6}	SDSS-DR5
6.81×10^{14}	2.25×10^{-3}	1.30×10^{-5}	XMM-*Newton* -OM
8.47×10^{14}	2.20×10^{-3}	9.06×10^{-6}	SDSS-DR5
1.05×10^{15}	1.00×10^{-3}	9.21×10^{-5}	IUE
1.46×10^{15}	5.25×10^{-4}	7.25×10^{-5}	IUE
2.11×10^{15}	1.45×10^{-4}	8.32×10^{-5}	IUE

Table B.6. Photometric data for PG 1247+267.

ν (Hz)	F_ν (Jy)	Error (Jy)	Ref.
1.49×10^{9}	1.17×10^{-3}	...	VLA (NED)
4.90×10^{9}	7.20×10^{-4}	8.00×10^{-5}	VLA (NED)
1.49×10^{10}	1.51×10^{-3}	2.20×10^{-4}	VLA (NED)
2.30×10^{11}	2.10×10^{-3}	...	IRAM (NED)
1.72×10^{12}	1.50×10^{-1}	...	ISO (NED)
2.93×10^{12}	1.74×10^{-1}	3.48×10^{-2}	ISO (NED)
4.93×10^{12}	2.36×10^{-1}	4.72×10^{-2}	ISO (NED)
1.20×10^{13}	1.13×10^{-1}	...	IRAS (NED)
2.34×10^{13}	3.00×10^{-2}	6.00×10^{-3}	ISO (NED)
3.91×10^{13}	1.00×10^{-2}	2.00×10^{-3}	ISO (NED)
6.17×10^{13}	9.00×10^{-3}	...	ISO (NED)
1.39×10^{14}	3.55×10^{-3}	1.36×10^{-4}	2MASS
1.80×10^{14}	2.99×10^{-3}	1.45×10^{-4}	2MASS
2.43×10^{14}	2.93×10^{-3}	1.10×10^{-4}	2MASS
3.33×10^{14}	6.31×10^{-3}	1.74×10^{-3}	SSS
3.28×10^{14}	3.01×10^{-3}	1.37×10^{-5}	SDSS-DR5
3.93×10^{14}	2.66×10^{-3}	9.69×10^{-6}	SDSS-DR5
4.28×10^{14}	4.03×10^{-3}	1.11×10^{-3}	SSS
4.81×10^{14}	2.26×10^{-3}	8.02×10^{-6}	SDSS-DR5
6.28×10^{14}	2.13×10^{-3}	6.42×10^{-6}	SDSS-DR5
6.81×10^{14}	3.54×10^{-3}	1.30×10^{-3}	SSS
8.47×10^{14}	2.27×10^{-3}	9.92×10^{-6}	SDSS-DR5
9.67×10^{14}	1.17×10^{-3}	8.00×10^{-6}	XMM-*Newton* -OM
1.25×10^{15}	6.70×10^{-4}	2.00×10^{-5}	XMM-*Newton* -OM
1.48×10^{15}	3.70×10^{-4}	2.00×10^{-5}	XMM-*Newton* -OM

Table B.7. Photometric data for IRAS F12509+3122.

ν (Hz)	F_ν (Jy)	Error (Jy)	Ref.
1.40×10^{9}	1.76×10^{-3}	1.25×10^{-4}	VLA (NED)
3.53×10^{11}	9.23×10^{-3}	...	SCUBA (Farrah et al. 2002a)
6.66×10^{11}	3.33×10^{-1}	...	SCUBA (Farrah et al. 2002a)
3.00×10^{12}	6.75×10^{-1}	...	IRAS (NED)
5.00×10^{12}	2.18×10^{-1}	4.36×10^{-2}	IRAS (NED)
1.20×10^{13}	1.03×10^{-1}	2.75×10^{-2}	IRAS (NED)
1.39×10^{14}	1.18×10^{-3}	8.78×10^{-5}	2MASS
1.80×10^{14}	7.75×10^{-4}	8.07×10^{-5}	2MASS
2.43×10^{14}	9.77×10^{-4}	6.01×10^{-5}	2MASS
3.33×10^{14}	8.60×10^{-4}	...	(Farrah et al. 2002a)
3.28×10^{14}	8.73×10^{-4}	7.57×10^{-6}	SDSS-DR5
3.93×10^{14}	8.39×10^{-4}	3.56×10^{-6}	SDSS-DR5
4.28×10^{14}	7.20×10^{-4}	7.00×10^{-5}	APM
4.81×10^{14}	8.39×10^{-4}	3.12×10^{-6}	SDSS-DR5
5.45×10^{14}	6.60×10^{-4}	1.60×10^{-5}	XMM-*Newton* -OM
6.28×10^{14}	8.32×10^{-4}	2.89×10^{-6}	SDSS-DR5
8.47×10^{14}	7.22×10^{-4}	4.89×10^{-6}	SDSS-DR5
9.67×10^{14}	4.94×10^{-4}	6.00×10^{-6}	XMM-*Newton* -OM
1.25×10^{15}	4.68×10^{-4}	7.00×10^{-6}	XMM-*Newton* -OM
1.33×10^{15}	7.83×10^{-4}	9.94×10^{-7}	HST - FOS
1.48×10^{15}	4.69×10^{-4}	1.60×10^{-5}	XMM-*Newton* -OM
1.75×10^{15}	5.16×10^{-4}	1.38×10^{-6}	HST - FOS

Table B.8. Photometric data for IRAS 12514+1027.

ν (Hz)	F_ν (Jy)	Error (Jy)	Ref.
1.40×10^{9}	7.78×10^{-3}	1.46×10^{-4}	VLA (NED)
3.00×10^{12}	7.55×10^{-1}	1.51×10^{-1}	IRAS (NED)
5.00×10^{12}	7.12×10^{-1}	5.70×10^{-2}	IRAS (NED)
1.20×10^{13}	1.90×10^{-1}	1.58×10^{-2}	IRAS (NED)
2.50×10^{13}	6.32×10^{-2}	...	IRAS (NED)
5.23×10^{13}	3.46×10^{-2}	4.03×10^{-3}	*Spitzer* -IRAC
8.44×10^{13}	1.49×10^{-2}	4.82×10^{-3}	*Spitzer* -IRAC
1.39×10^{14}	2.57×10^{-3}	1.26×10^{-4}	2MASS
1.80×10^{14}	8.45×10^{-4}	8.57×10^{-5}	2MASS
2.43×10^{14}	4.07×10^{-4}	5.40×10^{-5}	2MASS
3.33×10^{14}	2.88×10^{-4}	7.96×10^{-5}	SSS
3.28×10^{14}	5.66×10^{-4}	1.15×10^{-5}	SDSS-DR5
3.93×10^{14}	3.39×10^{-4}	2.96×10^{-6}	SDSS-DR5
4.28×10^{14}	2.46×10^{-4}	6.81×10^{-5}	SSS
4.81×10^{14}	2.82×10^{-4}	2.30×10^{-6}	SDSS-DR5
6.28×10^{14}	1.16×10^{-4}	1.50×10^{-6}	SDSS-DR5
6.81×10^{14}	5.78×10^{-5}	2.13×10^{-5}	SSS
8.47×10^{14}	4.79×10^{-5}	3.53×10^{-6}	SDSS-DR5

Table B.9. Photometric data for IRAS 14026+4341.

ν (Hz)	F_ν (Jy)	Error (Jy)	Ref.
1.40×10^{9}	1.59×10^{-3}	1.39×10^{-4}	VLA (NED)
3.53×10^{11}	7.53×10^{-3}	...	SCUBA (Farrah et al. 2002a)
6.66×10^{11}	9.40×10^{-2}	...	SCUBA (Farrah et al. 2002a)
3.00×10^{12}	9.94×10^{-1}	2.39×10^{-1}	IRAS (NED)
5.00×10^{12}	6.22×10^{-1}	5.60×10^{-2}	IRAS (NED)
1.20×10^{13}	2.85×10^{-1}	1.41×10^{-2}	IRAS (NED)
2.50×10^{13}	1.18×10^{-1}	2.71×10^{-2}	IRAS (NED)
3.91×10^{13}	3.60×10^{-2}	4.00×10^{-3}	ISO (NED)
7.05×10^{13}	1.60×10^{-2}	...	ISO (NED)
1.39×10^{14}	8.47×10^{-3}	2.29×10^{-4}	2MASS
1.80×10^{14}	4.75×10^{-3}	1.57×10^{-4}	2MASS
2.43×10^{14}	3.33×10^{-3}	1.01×10^{-4}	2MASS
3.33×10^{14}	2.26×10^{-3}	6.25×10^{-4}	SSS
3.28×10^{14}	3.83×10^{-3}	2.05×10^{-5}	SDSS-DR5
3.93×10^{14}	2.70×10^{-3}	1.23×10^{-5}	SDSS-DR5
4.81×10^{14}	2.82×10^{-3}	1.17×10^{-5}	SDSS-DR5
5.45×10^{14}	2.44×10^{-3}	1.90×10^{-5}	XMM-*Newton* -OM
6.28×10^{14}	2.09×10^{-3}	9.05×10^{-6}	SDSS-DR5
8.47×10^{14}	1.30×10^{-3}	7.19×10^{-6}	SDSS-DR5
9.67×10^{14}	7.70×10^{-4}	4.00×10^{-6}	XMM-*Newton* -OM
1.25×10^{15}	2.65×10^{-4}	7.00×10^{-6}	XMM-*Newton* -OM
1.48×10^{15}	1.59×10^{-4}	9.00×10^{-6}	XMM-*Newton* -OM
8.46×10^{16}	1.42×10^{-10}	8.39×10^{-10}	2XMMi
1.81×10^{17}	2.14×10^{-10}	3.50×10^{-10}	2XMMi
3.63×10^{17}	7.82×10^{-10}	3.76×10^{-10}	2XMMi
7.86×10^{17}	6.81×10^{-10}	3.85×10^{-10}	2XMMi
1.99×10^{18}	5.49×10^{-10}	5.17×10^{-10}	2XMMi

Table B.10. Photometric data for IRAS F14218+3845.

ν (Hz)	F_ν (Jy)	Error (Jy)	Ref.
3.53×10^{11}	8.55×10^{-3}	...	SCUBA (Farrah et al. 2002a)
6.66×10^{11}	2.53×10^{-1}	...	SCUBA (Farrah et al. 2002a)
3.15×10^{12}	1.64×10^{-1}	6.10×10^{-2}	ISO (NED)
2.00×10^{13}	3.23×10^{-3}	1.04×10^{-3}	ISO (NED)
4.44×10^{13}	7.90×10^{-4}	2.60×10^{-4}	ISO (NED)
3.33×10^{14}	5.00×10^{-5}	...	(Farrah et al. 2002a)
3.28×10^{14}	7.97×10^{-5}	4.34×10^{-6}	SDSS-DR5
3.93×10^{14}	9.09×10^{-5}	1.26×10^{-6}	SDSS-DR5
4.28×10^{14}	1.14×10^{-4}	1.05×10^{-5}	APM
4.81×10^{14}	1.01×10^{-4}	1.02×10^{-6}	SDSS-DR5
6.28×10^{14}	8.52×10^{-5}	7.85×10^{-7}	SDSS-DR5
8.47×10^{14}	8.47×10^{-5}	2.26×10^{-6}	SDSS-DR5

Table B.11. Photometric data for IRAS F15307+3252.

ν (Hz)	F_ν (Jy)	Error (Jy)	Ref.
1.40×10^{9}	5.71×10^{-3}	1.09×10^{-4}	VLA (NED)
8.42×10^{9}	9.20×10^{-4}	4.00×10^{-5}	VLA (NED)
1.02×10^{11}	4.50×10^{-2}	...	OVMA (NED)
2.39×10^{11}	5.10×10^{-3}	...	OVMA (NED)
3.53×10^{11}	1.15×10^{-2}	...	SCUBA (Farrah et al. 2002a)
6.66×10^{11}	1.06×10^{-1}	...	SCUBA (Farrah et al. 2002a)
1.66×10^{12}	4.14×10^{-1}	1.76×10^{-1}	ISO (NED)
3.00×10^{12}	5.10×10^{-1}	6.20×10^{-2}	IRAS (NED)
3.15×10^{12}	3.68×10^{-1}	1.16×10^{-1}	ISO (NED)
5.00×10^{12}	2.80×10^{-1}	2.70×10^{-2}	IRAS (NED)
1.20×10^{13}	8.00×10^{-2}	2.40×10^{-2}	IRAS (NED)
1.26×10^{13}	5.70×10^{-2}	3.00×10^{-3}	*Spitzer* -IRAC
2.50×10^{13}	4.50×10^{-2}	...	IRAS (NED)
1.39×10^{14}	3.20×10^{-4}	3.00×10^{-5}	MMT (NED)
1.80×10^{14}	1.68×10^{-4}	1.40×10^{-5}	MMT (NED)
2.43×10^{14}	1.48×10^{-4}	1.20×10^{-5}	MMT (NED)
3.33×10^{14}	6.70×10^{-5}	1.85×10^{-5}	SSS
3.28×10^{14}	1.28×10^{-4}	3.91×10^{-6}	SDSS-DR5
3.93×10^{14}	7.17×10^{-5}	1.06×10^{-6}	SDSS-DR5
4.28×10^{14}	6.32×10^{-5}	1.75×10^{-5}	SSS
4.81×10^{14}	5.90×10^{-5}	8.70×10^{-7}	SDSS-DR5
6.28×10^{14}	4.40×10^{-5}	6.89×10^{-7}	SDSS-DR5
6.81×10^{14}	3.40×10^{-5}	4.00×10^{-6}	XMM-*Newton* -OM
8.21×10^{14}	2.90×10^{-5}	2.00×10^{-6}	XMM-*Newton* -OM
8.47×10^{14}	3.34×10^{-5}	1.69×10^{-6}	SDSS-DR5
9.67×10^{14}	3.00×10^{-5}	2.00×10^{-6}	XMM-*Newton* -OM
1.48×10^{15}	1.90×10^{-5}	6.00×10^{-6}	XMM-*Newton* -OM

Table B.12. Photometric data for IRAS 16347+7037.

ν (Hz)	F_ν (Jy)	Error (Jy)	Ref.
1.45×10^{9}	9.40×10^{-4}	3.00×10^{-4}	VLA (NED)
1.49×10^{9}	1.65×10^{-3}	3.10×10^{-4}	VLA (NED)
4.90×10^{9}	1.08×10^{-3}	1.10×10^{-4}	VLA (NED)
8.48×10^{9}	9.70×10^{-4}	1.50×10^{-4}	VLA (NED)
1.49×10^{10}	1.17×10^{-3}	3.20×10^{-4}	VLA (NED)
2.25×10^{10}	9.60×10^{-4}	1.70×10^{-4}	VLA (NED)
4.00×10^{10}	2.78×10^{-1}	...	FCRAO (NED)
9.00×10^{10}	4.50×10^{-2}	...	NRAO-12m (NED)
2.30×10^{11}	1.50×10^{-3}	...	IRAM (NED)
1.48×10^{12}	1.58×10^{-1}	3.16×10^{-2}	ISO (NED)
1.72×10^{12}	2.06×10^{-1}	4.12×10^{-2}	ISO (NED)
1.93×10^{12}	2.30×10^{-1}	4.60×10^{-2}	ISO (NED)
2.93×10^{12}	3.49×10^{-1}	6.98×10^{-2}	ISO (NED)
5.00×10^{12}	2.46×10^{-1}	3.20×10^{-2}	IRAS (NED)
1.20×10^{13}	1.22×10^{-1}	4.15×10^{-3}	IRAS (NED)
2.50×10^{13}	5.93×10^{-2}	1.01×10^{-2}	IRAS (NED)
2.52×10^{13}	4.80×10^{-2}	9.60×10^{-3}	ISO (NED)
2.97×10^{13}	4.90×10^{-2}	1.10×10^{-2}	Hale-5m (Neugebauer et al. 1987)
8.10×10^{13}	1.07×10^{-2}	9.48×10^{-4}	Hale-5m (Neugebauer et al. 1987)
1.39×10^{14}	6.99×10^{-3}	2.13×10^{-4}	2MASS
1.80×10^{14}	8.91×10^{-3}	2.75×10^{-4}	2MASS
2.43×10^{14}	6.96×10^{-3}	2.06×10^{-4}	2MASS
3.33×10^{14}	7.07×10^{-3}	1.95×10^{-3}	SSS
4.28×10^{14}	7.27×10^{-3}	2.01×10^{-3}	SSS
5.45×10^{14}	4.76×10^{-3}	4.00×10^{-5}	XMM-*Newton* -OM
6.81×10^{14}	6.20×10^{-3}	2.28×10^{-3}	SSS
8.21×10^{14}	3.71×10^{-3}	1.60×10^{-5}	XMM-*Newton* -OM
1.05×10^{15}	3.77×10^{-3}	4.97×10^{-6}	IUE
1.46×10^{15}	1.22×10^{-3}	4.71×10^{-6}	IUE
1.48×10^{15}	1.59×10^{-3}	6.00×10^{-5}	XMM-*Newton* -OM
2.11×10^{15}	4.60×10^{-4}	8.92×10^{-6}	IUE

Table B.13. Photometric data for IRAS 18216+6418.

ν (Hz)	F_ν (Jy)	Error (Jy)	Ref.
3.25×10^{8}	2.11×10^{-1}	9.65×10^{-3}	WENSS (NED)
4.90×10^{9}	7.50×10^{-3}	4.00×10^{-4}	VLA (NED)
8.42×10^{9}	1.26×10^{-2}	6.00×10^{-4}	VLA (NED)
1.49×10^{10}	2.33×10^{-2}	1.10×10^{-3}	VLA (NED)
2.39×10^{11}	3.70×10^{-3}	...	(Farrah et al. 2002a)
2.73×10^{11}	4.70×10^{-2}	...	(Farrah et al. 2002a)
3.53×10^{11}	1.48×10^{-2}	2.60×10^{-3}	SCUBA (Farrah et al. 2002a)
6.66×10^{11}	3.08×10^{-1}	...	SCUBA (Farrah et al. 2002a)
1.72×10^{12}	1.07×10^{0}	3.21×10^{-1}	ISO (NED)
3.00×10^{12}	2.13×10^{0}	1.70×10^{-1}	IRAS (NED)
5.00×10^{12}	1.24×10^{0}	4.96×10^{-2}	IRAS (NED)
1.20×10^{13}	4.45×10^{-1}	1.19×10^{-2}	IRAS (NED)
2.50×10^{13}	2.38×10^{-1}	...	IRAS (NED)
3.12×10^{13}	1.43×10^{-1}	1.43×10^{-2}	ISO (NED)
4.44×10^{13}	1.09×10^{-1}	1.10×10^{-2}	ISO (NED)
1.39×10^{14}	2.35×10^{-2}	6.04×10^{-4}	2MASS
1.80×10^{14}	1.47×10^{-2}	4.25×10^{-4}	2MASS
2.43×10^{14}	1.19×10^{-2}	3.18×10^{-4}	2MASS
3.33×10^{14}	1.69×10^{-2}	4.68×10^{-3}	SSS
4.28×10^{14}	1.24×10^{-2}	3.42×10^{-3}	SSS
5.45×10^{14}	7.55×10^{-3}	...	(Farrah et al. 2002a)
6.81×10^{14}	8.10×10^{-3}	7.00×10^{-4}	APM
8.21×10^{14}	9.04×10^{-3}	...	(Farrah et al. 2002a)
1.48×10^{15}	4.94×10^{-3}	6.00×10^{-5}	XMM-*Newton* -OM